Emergence of Elastostatic Strain-Gradient Effects from Topological Optimization

Valentin Calisti, Arthur Lebée, A A Novotny, J Sokolowski

EMERGENCE OF ELASTOSTATIC STRAIN-GRADIENT EFFECTS FROM TOPOLOGICAL OPTIMIZATION

V. CALISTI, A. LEBÉE, A.A. NOVOTNY, AND J. SOKOLOWSKI

Abstract. There are very few examples of architectured materials producing significant strain-gradient effects in elastostatics. In the present paper, we generate for the first time new microstructures featuring these effects from topological optimization of two-dimensional periodic media. The optimized shape functionals depend on the first and second-order homogenized tensors, obtained from the two-scale asymptotic expansion homogenization scheme.

The optimization method relies on the recently rigorously derived topological derivative of the second-order homogenized tensor, measuring the strain-gradient sensitivity with respect to a small circular inclusion at the microscopic level endowed with different material property from the background.

Keywords: Topological optimization, Higher-order homogenization, Strain-gradient continuum, Architectured materials, Periodic homogenization.

1. Introduction

Additive manufacturing and topological optimization sparked a renewed interest in the study of *architectured materials* over the past two decades, partly due to the emergence of 3D printers and the improvement of the computational methods and power. In the present study, we are interested in two dimensional continuous periodic materials, designed in such a way that the required macroscopic properties are obtained after organizing their inner microstructure. The framework describing macroscopic properties of a material from the analysis of its microstructure, called *homogenization*, usually allows to describe an architectured material by an approximated first-gradient macroscopic model. Namely, the sole first gradient of the macroscopic displacement field is used for measuring the elastic energy. Such models have been extensively studied and optimized (see (Amstutz et al., 2010; Bendsøe and Sigmund, 2003; Wang et al., 2014), among others), but they are valid under a hypothesis of scale separation and finite contrast.

However, this hypothesis may not be satisfied in practice. In this case, other macroscopic models also called *generalized continua* are needed, such as higher order models, having additional degrees of freedom (for instance *Cosserat materials*), or higher gradient models for which higher-order gradient of the macroscopic displacement field are used for measuring the elastic energy (see e.g., (Forest, 2006)). Thus, we explore how to produce new microstructures yielding non-classical and interesting behavior, and how to optimize these effects. In particular, we study the numerical synthesis of novel periodic continuous microstuctures featuring higher gradient macroscopic effects, and more precisely strain-gradient effects.

In dynamics, strain-gradient elasticity is relevant when the wavelength is of the same order as the size of the heterogeneities of a material, leading for example to new dispersive properties (see e.g., (Rosi and Auffray, 2016)). In an effort to improve these effects, the shape and topological optimization have been investigated for wave equations in periodic structures, some based on the shape sensitivity (Allaire and Yamada, 2018), others on the topological sensitivity (Bonnet et al., 2018; Cornaggia and Bellis, 2020).

In elastostatics, the macroscopic length scale is typically the size of the domain and strain-gradient effects may be understood as small corrections of classical elasticity. Hence, contrary

Date: January 12, 2024.

to dynamics, they are difficult to observe unless some specific stiffness contrast assumptions are made. Indeed, it was shown theoretically in (Camar-Eddine and Seppecher, 2003) that many different models of generalized continua can be obtained from the homogenization of a mixture of materials with large contrast and some microstructures were investigated in this framework (see (Alibert et al., 2003; Abdoul-Anziz et al., 2019), among others). Nevertheless, in practice, there are not so many microstructures that result in a generalized continuum for the elastostatic case. For this reason, we generate such microstructures in the present work. Instead of making assumptions on the contrast of the materials, we use topological optimization to produce non-classical effects arising from geometrical contrasts. In particular, we focus on the optimization of strain-gradient effects in elastostatics.

For this, we rely on the classical two-scale asymptotic expansion method, which brings out higher-gradient terms as corrections of the first-gradient elasticity, and allows to identify the higher-order homogenized tensors by computing the macroscopic elastic energy. In (Smyshlyaev and Cherednichenko, 2000), a higher order convergence result is given for an infinite periodic media with a finite material contrast. Although the assumptions are restrictive, this result gives an interesting heuristic, and has been used in (Durand et al., 2022) to detect strain-gradient effects in a material with voids inclusions by a numerical investigation. To achieve this result, the first-gradient homogenized tensor should be degenerated to create zero-energy modes, so that the strain-gradient terms, which are usually small correction terms, become predominant. Thus, we follow such an approach in order to maximize strain-gradient effects in periodic media, for which the unit cell is a mixture of two elastic materials with a property contrast.

In order to produce some new microstructures, a possible strategy is to use shape or topological optimization methods, which have been widely applied to structural optimization problems (see e.g., (van Dijk et al., 2013; Rozvany, 2009) for reviews, and (Allaire, 2002; Sigmund and Maute, 2013) for detailed introductions), as well as to many other fields, such as imaging, fluid mechanics, heat conduction problems, acoustic, electromagnetic, inverse problems, and piezoelectric. Among the main ones, we can mention the *evolutionary approaches* (see e.g., (Allaire, 2007)), *phase-field* approaches (see e.g., (Wallin et al., 2012)), the *density methods* (such as the homogenization approach (Allaire, 2002), or the SIMP method (Bendsøe, 1989; Zhou and Rozvany, 1991)), and the *level-set methods* (introduced in (Osher and Sethian, 1988), see e.g. (van Dijk et al., 2013) for a review).

In this paper the topological derivative method is adopted. In contrast to the above mentioned methods, the topological derivative has been specifically conceived to provide a precise information on the sensitivity of a given shape functional with respect to topological domain perturbations. The origin of the topological derivative method in optimal design can be dated to the work by Schumacher et al. (Eschenauer et al., 1994; Schumacher, 1996) on the optimal location of holes within elastic structures. The first mathematical justifications for topological derivatives in the framework of partial differential equations are due to Sokołowski and Żochowski (1999) and Garreau et al. (2001), in the context of the Poisson equation and the Navier system for Neumann and Dirichlet holes. Therefore, this relatively new concept in shape optimization has applications in many different fields such as shape and topology optimization, geometrical inverse problems, image processing, multi-scale material design and mechanical modelling, including damage and fracture evolution phenomena. See, for instance, the book (Novotny et al., 2019) and the special issue on the topological derivative method and its applications in computational engineering (Novotny et al., 2022), covering various topics ranging from new theoretical developments up to industrial applications.

Concerning architectured materials, this method has already been used in (Amstutz et al., 2010) for periodic media made of the mixture of two materials, whose macroscopic behaviours are described by first-gradient models. In the present paper, we are interested in the synthesis of periodic media, which feature significant strain-gradient effects.

Thus, we use the topological derivatives of the related higher-order homogenized tensors which were derived in (Calisti et al., 2021), in order to tackle numerically the problem. The synthesis of periodic media is made by optimizing the distribution of the two materials, in Ω and $\mathcal{Y} \setminus \overline{\Omega}$, composing the unit cell $\mathcal{Y}$. For this, we optimize the homogenized tensors $\mathrm{C}^h(\Omega)$ and $\mathrm{D}^h(\Omega)$, carrying respectively the strain and the strain gradient terms in the macroscopic elastic energy, and depending on the distribution of material. Hence, we numerically investigate the following problem:

$$\min_{\Omega} \left\{ \mathcal{J}(\mathrm{C}^h(\Omega), \mathrm{D}^h(\Omega)) \right\}, \tag{1.1}$$

where $\mathcal{J}$ is a shape functional depending on Ω through the homogenized tensors. The effective mechanical properties contained in the fourth order tensor $\mathrm{C}^h(\Omega)$ are known. However it is not trivial to derive from the higher-order tensor $\mathrm{D}^h(\Omega)$ some coefficients being meaningful from a mechanical point of view. The approach we follow in this study is based on some natural characteristic intrinsic lengths defined as square roots of ratios between the components of the homogenized tensors: $(\mathrm{D}^h_{ijklmn}(\Omega)/\mathrm{C}^h_{ijlm}(\Omega))^{1/2}$. From the point of view of shape and topology optimization the shape functional actually depends on the characteristic function of $\Omega \subset \mathcal{Y}$.

The paper is organized as follows. In Section 2, we start by introducing the framework of microstructure optimization. We present the homogenization scheme, based on the *asymptotic expansion method*, allowing us to define the so-called higher homogenized tensors, which encapsulate information about the macroscopic properties of this material. Then, the topological derivative is presented in Section 3. We describe the topological perturbation of the problem, and recall the topological derivatives of higher order homogenized tensors which were derived in (Giusti et al., 2009b) and (Calisti et al., 2021). The latter measure how the homogenized tensors change when a small circular inclusion is introduced at the microscale level. In Section 4, we present the gradient type algorithm based on these topological derivatives, that we use in Section 5 in order to investigate the maximization of characteristic lengths, and generate new microstructures featuring strain-gradient effects.

2. Higher-order homogenized tensors from the two-scale asymptotic expansion

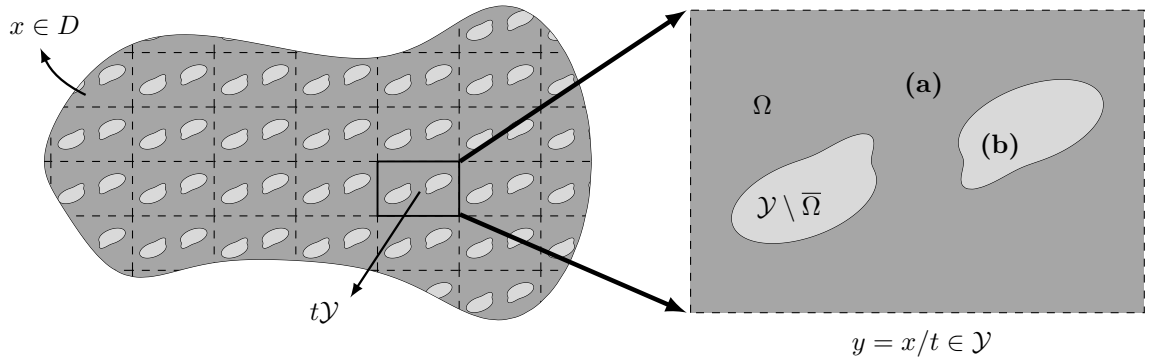

Figure 1. The domain D is paved with the unit cell domain $\mathcal{Y}$, weighted by the length parameter t. The unit cell is composed of two different materials, a stiff material **(a)** and a soft material **(b)**, represented respectively by the domains Ω and $\mathcal{Y} \setminus \overline{\Omega}$.

Let D be a connected bounded regular open subset of $\mathbb{R}^2$ representing an elastic body having a periodic micro-structure (see Figure 1). We assume that this material is a *first-gradient material*, completely characterized by its *elasticity tensor*.

2.1. **The unit cell $\mathcal{Y}$.** Let $\{\mathrm{e}_1, \mathrm{e}_2\}$ be an orthonormal basis of $\mathbb{R}^2$, and

$$\mathcal{Y} = (0, l_1) \times (0, l_2) \tag{2.1}$$

be an open rectangle of $\mathbb{R}^2$, for $0 < l_1, l_2$. The open set $\mathcal{Y}$ stands for the *unit cell* of the periodic material. We assume that this unit cell $\mathcal{Y}$ is composed of two different homogeneous and isotropic elastic materials: a stiff material **(a)**, and a soft material **(b)**. The stiff material occupies an open subset Ω of $\mathcal{Y}$, and the soft material occupies the complementary domain $\mathcal{Y} \setminus \overline{\Omega}$ in the unit cell (see Figure 1). These two elastic materials are characterized by the same *Poisson's coefficient* ν, and by *Young's moduli* differing from a ratio $0 < \gamma_0 < +\infty$, where γ_0 is called the *contrast* of elastic properties between the two materials. Let C_0 be the constant elasticity tensor describing the stiff elastic material **(a)**, defined by

$$\mathrm{C}_0 = \frac{E}{1-\nu^2}\left((1-\nu)\mathbb{I} + \nu \mathrm{I} \otimes \mathrm{I}\right), \tag{2.2}$$

where E is the Young's modulus of the stiff elastic material. The tensor $\mathrm{I} = \mathrm{e}_i \otimes \mathrm{e}_i$ is the identity second order tensor, and $\mathbb{I}$ the fourth order symmetric identity tensor. They are defined by

$$\mathrm{I}_{ij} = \delta_{ij}, \tag{2.3}$$

$$\mathbb{I}_{ijkl} = \frac{1}{2}(\delta_{ik}\delta_{jl} + \delta_{il}\delta_{jk}), \tag{2.4}$$

δ_{ij} being the Kronecker symbol. Then we can write the elasticity tensor characterizing the unit cell $\mathcal{Y}$. The two phases of material result in a piecewise constant fourth order tensor $\mathrm{C} = (\mathrm{C}_{ijkl})_{1 \le i,j,k,l \le 2}$, which is defined as follows

$$\mathrm{C}(y) := \begin{cases} \mathrm{C}_0, & y \in \Omega, \\ \gamma_0 \mathrm{C}_0, & y \in \mathcal{Y} \setminus \overline{\Omega}. \end{cases} \tag{2.5}$$

Before going further in the description of the model, we write the convention we use for tensor calculus. Let u and v be two vectors of $\mathbb{R}^2$, A and B be two second order tensors of $\mathbb{R}^2$, C and D be two third order tensors, E be a fourth order tensor, and F be a sixth order tensor, we write:

$$FC = F_{ijklmn} C_{lmn}\, \mathrm{e}_i \otimes \mathrm{e}_j \otimes \mathrm{e}_k, \qquad EA = E_{ijkl} A_{kl}\, \mathrm{e}_i \otimes \mathrm{e}_j, \tag{2.6}$$

$$AB = A_{ik} B_{kj}\, \mathrm{e}_i \otimes \mathrm{e}_j, \qquad Au = A_{ij} u_j\, \mathrm{e}_i, \tag{2.7}$$

$$C \cdot D = C_{ijk} D_{ijk}, \qquad A \cdot B = A_{ij} B_{ij}, \tag{2.8}$$

$$u \cdot v = u_i v_i, \tag{2.9}$$

by using the Einstein summation convention, and where $\mathrm{e}_i \otimes \mathrm{e}_j$ is a matrix such that $(\mathrm{e}_i \otimes \mathrm{e}_j)_{kl} = \delta_{ik}\delta_{jl}$. We finally define

$$u \otimes_s v := \frac{u \otimes v + v \otimes u}{2}. \tag{2.10}$$

2.2. **The periodic body.** The elasticity tensor characterizing the elastic body D is now defined. Let $0 < t$ be a microscopic length parameter describing the length-scale of the microscopic variations of the elasticity tensor, and let $0 < T$ be a macroscopic length parameter which can be for example defined by $T = \mathrm{diam}(D)$, such that $t \ll T$. We denote by τ the scale ratio

$$\tau = t/T. \tag{2.11}$$

For convenience, we assume that $T = 1$, and thus $\tau = t \ll 1$. Actually, the periodic medium we are interested in, consists of the domain D, which is paved with the *microscopic periodic cell* $\tau\mathcal{Y}$ (see Figure 1). Thus we define the elasticity tensor of the periodic material D, depending on the parameter τ, as follows:

$$\mathrm{C}^\tau(x) := \mathrm{C}(x/\tau), \tag{2.12}$$

where C is defined in (2.5). We notice that the tensor C^τ of microscopic moduli does not depend on the macroscale position $Y := x$, but only on the microscale variable $y := x/\tau$.

This material is subjected to *body forces* $f \in L^2(D)$, and the *displacement field* $u^\tau : D \to \mathbb{R}^2$, which is the unknown of the problem, is fixed on the boundary ∂D. The displacement vector field u^τ is then given by the solution of the following boundary value problem of linearized elasticity

$$\begin{cases} -\operatorname{div}_x(\sigma_x^\tau(u^\tau)) = f & \text{in } D, \\ u^\tau = 0 & \text{on } \partial D, \end{cases} \tag{2.13}$$

where the second order tensor field $\sigma_x^\tau(u^\tau)$ is the *stress tensor*, defined throughout the following constitutive stress-strain relation in the linear elastic regime:

$$\sigma_x^\tau(u^\tau) := \mathrm{C}^\tau \varepsilon_x(u^\tau), \tag{2.14}$$

$$\varepsilon_x(u^\tau) := \nabla_x^s u^\tau := \frac{1}{2}\left(\nabla_x(u^\tau) + \nabla_x(u^\tau)^\top\right), \tag{2.15}$$

where the right lower index of a differential operator denotes the differentiation variable, and where $\varepsilon_x(u^\tau)$ is the *linearized strain tensor*.

2.3. **The homogenized material and homogenized tensors.** The two-scale asymptotic expansion method is used to define the higher-order homogenized tensors. The interested reader can refer to (Calisti et al., 2021) for more details and references.

2.3.1. *Second-order truncation, definition of the homogenized tensors.* We define

$$y = x/\tau \quad \text{and} \quad Y = x, \tag{2.16}$$

respectively the microscopic and macroscopic variables, for all $x \in D$ (see Figure 1). The method relies on an asymptotic expansion of the displacement flied with respect to the scale ratio τ, by using corrector fields depending on both the macroscopic vairiable and the microscopic variable. From this, the displacement field is approximated by a truncation of this expansion. In the present case, we consider the following truncation up to the second order of the parameter τ:

$$\bar{u}^\tau(Y, y) = U(Y) + \tau\, h_{ij}^1(y) E_{ij}(Y) + \tau^2\, h_{ijk}^2(y) K_{ijk}(Y), \tag{2.17}$$

where $E(Y) = \nabla^s U(Y)$ is the macroscopic strain, and $K(Y) = \nabla E(Y)$ is the corresponding strain-gradient. The displacement corrector fields h_{ij}^1 and h_{ijk}^2 are respectively solutions of the following canonical set of variational problems (see (Calisti et al., 2021))

$$h_{ij}^1 \in \mathcal{V} \ : \ \int_{\mathcal{Y}} \sigma_y(h_{ij}^1) \cdot \varepsilon_y(\eta) + \int_{\mathcal{Y}} \mathrm{C}(\mathrm{e}_i \otimes_s \mathrm{e}_j) \cdot \varepsilon_y(\eta) = 0, \quad \forall \eta \in \mathcal{W}, \tag{2.18}$$

and

$$h_{ijk}^2 \in \mathcal{V} \ : \ \int_{\mathcal{Y}} \sigma_y(h_{ijk}^2) \cdot \varepsilon_y(\eta) + \int_{\mathcal{Y}} \mathrm{C}(h_{ij}^1 \otimes_s \mathrm{e}_k) \cdot \varepsilon_y(\eta) = \int_{\mathcal{Y}} (\sigma_y(u_{ij}) - \mathrm{C}^h(\mathrm{e}_i \otimes_s \mathrm{e}_j))\mathrm{e}_k \cdot \eta, \quad \forall \eta \in \mathcal{W}, \tag{2.19}$$

where u_{ij} and C^h are respectively given in (2.26) and (2.29) below, $\sigma_y(h_{ij}^1) = \mathrm{C}\varepsilon_y(h_{ij}^1)$, and the spaces $\mathcal{W}$ and $\mathcal{V}$ are defined as follows

$$\mathcal{W} := H^1_{\mathrm{per}}(\mathcal{Y}; \mathbb{R}^2)/\mathbb{R}, \tag{2.20}$$

$$\mathcal{V} := \left\{ \eta \in H^1_{\mathrm{per}}(\mathcal{Y}; \mathbb{R}^2) \ : \ \langle \eta \rangle = 0 \right\}. \tag{2.21}$$

Here for all tensor fields A, we define the *volume averaging* of A

$$\langle A \rangle := \frac{1}{|\mathcal{Y}|} \int_{\mathcal{Y}} A(y) dy, \tag{2.22}$$

where $|\mathcal{Y}|$ denotes the area of the unit cell.

From this, we define the approximated macroscopic energy $\mathscr{E}^h(\bar{u}^\tau)$ as being the average of the microscopic elastic energy $\mathscr{E}_\mu(\bar{u}^\tau)$ on the unit cell domain $\mathcal{Y}$ defined by

$$\mathscr{E}_\mu(\bar{u}^\tau) = \frac{1}{2}\sigma_x(\bar{u}^\tau)\cdot\varepsilon_x(\bar{u}^\tau), \tag{2.23}$$

so that

$$\mathscr{E}^h(\bar{u}^\tau) = \frac{1}{|\mathcal{Y}|}\int_{\mathcal{Y}}\frac{1}{2}\sigma_x(\bar{u}^\tau)\cdot\varepsilon_x(\bar{u}^\tau)\,dy = \left\langle\frac{1}{2}\sigma_x\cdot\varepsilon_x\right\rangle. \tag{2.24}$$

By calculating the strain tensor induced by $\bar{u}^\tau$, we find

$$\varepsilon_x(\bar{u}^\tau) = \varepsilon_y(u_{ij})E_{ij} + \tau(h^1_{ij}\otimes_s \mathrm{e}_k + \varepsilon_y(h^2_{ijk}))K_{ijk} + \tau^2(h^2_{ijk}\otimes_s \mathrm{e}_l)\partial_{Y_l}K_{ijk}, \tag{2.25}$$

where u_{ij} is given by

$$u_{ij}(y) := (\mathrm{e}_i\otimes_s \mathrm{e}_j)y + h^1_{ij}(y). \tag{2.26}$$

Then we can compute $\frac{1}{2}\sigma_x(\bar{u}^\tau)\cdot\varepsilon_x(\bar{u}^\tau)$, and evaluate the truncated homogenized energy $\mathscr{E}^h(\bar{u}^\tau)$ defined by (2.24). The expression of $\mathscr{E}^h(\bar{u}^\tau)$ allows to identify the homogenized tensors, which are thus defined as integrals over the cell $\mathcal{Y}$ of products of the fields depending on the microscopic variable y in expression (2.25). This gives the following expression

$$2\mathscr{E}^h = E_{ij}\mathrm{C}^h_{ijkl}E_{kl} + \tau E_{ij}\mathrm{E}^h_{ijpqr}K_{pqr} + \tau^2(K_{ijk}\mathrm{F}^h_{ijkpqr}K_{pqr} + 2E_{ij}\mathrm{G}^h_{ijkpqr}\partial_{Y_k}K_{pqr}) + o(\tau^2), \tag{2.27}$$

in which C^h, E^h, F^h and G^h are so-called homogenized tensors. The energy depends on the gradient of the strain-gradient ∇K at order τ^2. In order to only deal with strain-gradient coupling effects, it is necessary to perform a macroscopic integration by part to transform the coupled terms $E_{ij}\partial_{y_k}K_{pqr}$ into $K_{ijk}K_{pqr}$. By doing this, we consider the bulk of the material D, and we do not take into account the boundary terms (see (Durand et al., 2022)). As a result, the truncated homogenized energy can be written as

$$\mathscr{E}^h = \frac{1}{2}E_{ij}\mathrm{C}^h_{ijkl}E_{kl} + \tau E_{ij}\mathrm{E}^h_{ijpqr}K_{pqr} + \tau^2\frac{1}{2}K_{ijk}\mathrm{D}^h_{ijkpqr}K_{pqr} + o(\tau^2), \tag{2.28}$$

where $\mathrm{D}^h = \mathrm{F}^h - 2\mathrm{G}^h$. In particular, we focus on the optimization of functionals depending only on the fourth order tensor $\mathrm{C}^h = (\mathrm{C}^h_{ijkl})_{1\le i,j,k,l\le 2}$, and the sixth order tensor $\mathrm{D}^h = (\mathrm{D}^h_{ijkpqr})_{1\le i,j,k,p,q,r\le 2}$, which are defined from (2.25), (2.24) and (2.28), and respectively given in index format by

$$\mathrm{C}^h_{ijkl} := \frac{1}{|\mathcal{Y}|}\int_{\mathcal{Y}}\sigma_y(u_{ij})\cdot\varepsilon_y(u_{kl}) = \langle\sigma_y(u_{ij})\cdot\varepsilon_y(u_{kl})\rangle, \tag{2.29}$$

and

$$\begin{aligned}\mathrm{D}^h_{ijkpqr} &:= \frac{1}{|\mathcal{Y}|}\int_{\mathcal{Y}}\mathrm{C}(h^1_{ij}\otimes_s \mathrm{e}_k + \varepsilon_y(h^2_{ijk}))\cdot(h^1_{pq}\otimes_s \mathrm{e}_r + \varepsilon_y(h^2_{pqr}))\\ &\qquad - \frac{1}{|\mathcal{Y}|}\int_{\mathcal{Y}}\Big(\sigma_y(u_{ij})\cdot(h^2_{pqr}\otimes_s \mathrm{e}_k) + \sigma_y(u_{pq})\cdot(h^2_{ijk}\otimes_s \mathrm{e}_r)\Big)\\ &:= \Big\langle\mathrm{C}(h^1_{ij}\otimes_s \mathrm{e}_k + \varepsilon_y(h^2_{ijk}))\cdot(h^1_{pq}\otimes_s \mathrm{e}_r + \varepsilon_y(h^2_{pqr}))\Big\rangle\\ &\qquad - \Big\langle\Big(\sigma_y(u_{ij})\cdot(h^2_{pqr}\otimes_s \mathrm{e}_k) + \sigma_y(u_{pq})\cdot(h^2_{ijk}\otimes_s \mathrm{e}_r)\Big)\Big\rangle.\end{aligned} \tag{2.30}$$

3. Topological Sensitivity

So far, we have defined the homogenized tensors C^h, and D^h. We are now interested in the optimization of the topology of the unit cell composing a periodic body, in order to improve some of its macroscopic properties by using the topological derivative method. We refer to the books (Novotny and Sokołowski, 2013), and (Novotny and Sokołowski, 2020) for a comprehensive introduction on the subject. For practical use and future investigations, we mention that the topological sensitivities of the homogenized tensors E^h, F^h and G^h were also computed in (Calisti, 2021).

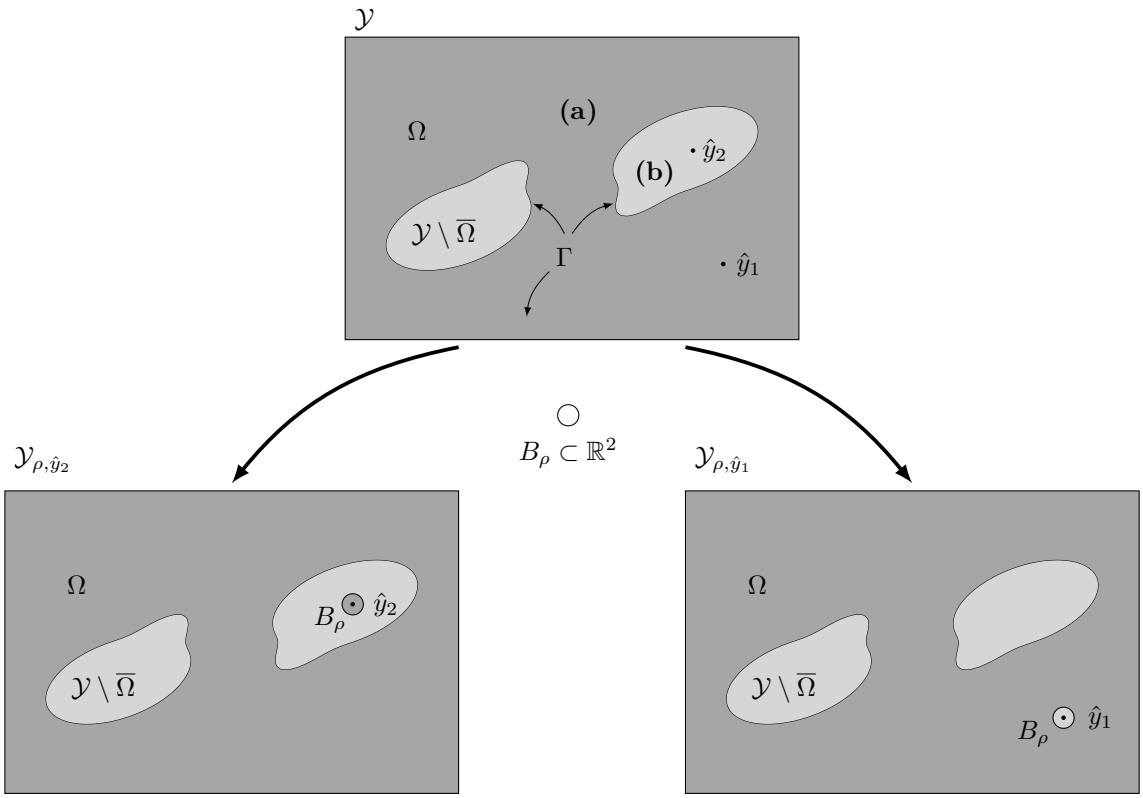

FIGURE 2. Introduction of an inclusion centered at $\hat{y}_1$ or $\hat{y}_2$ into the domains Ω or $\mathcal{Y}\setminus\overline{\Omega}$ respectively. The resulting domains are denoted by $\mathcal{Y}_{\rho,\hat{y}_1}$ and $\mathcal{Y}_{\rho,\hat{y}_2}$.

3.1. **Perturbation of the unit cell.** We consider the unit cell of a periodic material $\mathcal{Y}$, which is made of a mixture of two materials, defined in Section 2.1. From there, $\mathcal{Y}$ is subjected to a perturbation confined in a small circular open set $B_\rho(\hat{y})$ of radius ρ and centered at an arbitrary point $\hat{y}$ of $\mathcal{Y}$, such that its closure is included in $\mathcal{Y}$, and which does not touch the interface Γ (see Figure 2). Then, the region occupied by $B_\rho(\hat{y})$ is filled by an inclusion with different material property from the background. The material properties of the perturbed domain are characterized by the piecewise constant function γ_ρ of the form

$$\gamma_\rho(x) := \begin{cases} 1 & \text{if } x \in \mathcal{Y}\setminus\overline{B_\rho}\,, \\ \gamma(x) & \text{if } x \in B_\rho\,, \end{cases} \tag{3.1}$$

where

$$\gamma(x) := \begin{cases} \gamma_0 & \text{if } x \in \Omega\,, \\ \gamma_0^{-1} & \text{if } x \in \mathcal{Y}\setminus\overline{\Omega}\,. \end{cases} \tag{3.2}$$

Namely we introduce either a small ball of soft material into the stiff one, or a small ball of stiff material into the soft one. Finally the elasticity tensor is given by $\gamma_\rho \mathrm{C}$ in the perturbed domain.

The topologically perturbed counterparts of problems (2.18) and (2.19) are respectively given by

$$h_{ij}^{1\,\rho} \in \mathcal{V} \;:\; \int_{\mathcal{Y}} \gamma_\rho \sigma(h_{ij}^{1\,\rho}) \cdot \varepsilon(\eta) = -\int_{\mathcal{Y}} \gamma_\rho \mathrm{C}(\mathrm{e}_i \otimes_s \mathrm{e}_j) \cdot \varepsilon(\eta), \quad \forall \eta \in \mathcal{W}, \tag{3.3}$$

and

$$h^2_{ijk}{}^\rho \in \mathcal{V} \ : \ \int_{\mathcal{Y}} \gamma_\rho \sigma(h^2_{ijk}{}^\rho) \cdot \varepsilon(\eta) = -\int_{\mathcal{Y}} \gamma_\rho \mathrm{C}(h^1_{ij}{}^\rho \otimes_s \mathrm{e}_k) \cdot \varepsilon(\eta) + \int_{\mathcal{Y}} (\gamma_\rho \sigma(u^\rho_{ij}) - \mathrm{C}^h_\rho(\mathrm{e}_i \otimes_s \mathrm{e}_j))\mathrm{e}_k \cdot \eta \quad \forall \eta \in \mathcal{W}, \quad (3.4)$$

where from now on we leave the lower indices of differential operators behind. As we did in Section 2, we can define the topologically perturbed counterparts of the homogenized tensors, denoted as C^h_ρ, and D^h_ρ. By setting

$$u^\rho_{ij} := (\mathrm{e}_i \otimes_s \mathrm{e}_j)y + h^1_{ij}{}^\rho, \quad (3.5)$$

which gives

$$(\mathrm{C}^h_\rho)_{ijkl} = \left\langle \gamma_\rho \sigma(u^\rho_{ij}) \cdot \varepsilon(u^\rho_{kl}) \right\rangle, \quad (3.6)$$

$$(\mathrm{D}^h_\rho)_{ijkpqr} = \left\langle \gamma_\rho \mathrm{C}(h^1_{ij}{}^\rho \otimes_s \mathrm{e}_k + \varepsilon(h^2_{ijk}{}^\rho)) \cdot (h^1_{pq}{}^\rho \otimes_s \mathrm{e}_r) \right\rangle - \left\langle (\mathrm{C}^h_\rho(\mathrm{e}_i \otimes_s \mathrm{e}_j) \cdot (h^2_{pqr}{}^\rho \otimes_s \mathrm{e}_k) + \gamma_\rho \sigma(u^\rho_{pq}) \cdot (h^2_{ijk}{}^\rho \otimes_s \mathrm{e}_r)) \right\rangle. \quad (3.7)$$

From there, we denote by $\mathcal{H}$ any homogenized tensor we are interested in, namely C^h or D^h. We assume that the following topological asymptotic expansion holds true

$$\mathcal{H}_\rho = \mathcal{H} + g(\rho) D_T \mathcal{H}(\hat{y}) + o(g(\rho)), \quad (3.8)$$

where g is a positive function, such that $g(\rho) \to 0$ with $\rho \to 0$. Then the function

$$\hat{y} \in \mathcal{O} \longmapsto D_T \mathcal{H}(\hat{y}) \quad (3.9)$$

is called the *topological derivative* of $\mathcal{H}$ at $\hat{y}$.

3.2. **Topological derivatives of the homogenized tensors.** In this section, we give the rigorous formulas of the topological derivatives of the homogenized elasticity tensors C^h (see (Giusti et al., 2009b)) and D^h. Unlike for C^h, the computation of topological derivative of D^h, requires the introduction of so-called *adjoint states* $p^r_{ijk} \in \mathcal{V}$ for $i, j, k, r \in \{1, 2\}$ (see (Calisti et al., 2021)). For C^h, the associated problem is self-adjoint, and then no Lagrangian need to be introduced. But the correctors h^1 and h^2 both involved in the definition of D^h are solutions of a coupling problem, which leads to the emergence of a Lagrangian and its associated adjoint states.

The topological asymptotic expansion of the homogenized tensors, then the topological derivatives of any component of tensors C^h and D^h are given by

$$(D_T \mathrm{C}^h)_{ijkl}(\hat{y}) = \mathbb{P}\sigma(u_{ij})(\hat{y}) \cdot \varepsilon(u_{kl})(\hat{y}), \quad (3.10)$$

and

$$\begin{aligned}(D_T \mathrm{D}^h)_{ijkpqr}(\hat{y}) = {} & \mathbb{P}(\sigma(h^2_{ijk})(\hat{y}) + \mathrm{C}(h^1_{ij}(\hat{y}) \otimes_s \mathrm{e}_k)) \cdot (\varepsilon(h^2_{pqr})(\hat{y}) + (h^1_{pq}(\hat{y}) \otimes_s \mathrm{e}_r)) \\ & - \mathbb{P}\sigma(u_{ij})(\hat{y}) \cdot (\varepsilon(p^k_{pqr})(\hat{y}) + (h^2_{pqr}(\hat{y}) \otimes_s \mathrm{e}_k)) \\ & - \mathbb{P}\sigma(u_{pq})(\hat{y}) \cdot (\varepsilon(p^r_{ijk})(\hat{y}) + (h^2_{ijk}(\hat{y}) \otimes_s \mathrm{e}_r)), \end{aligned} \quad (3.11)$$

where $\hat{y}$ is the location of the perturbation, u_{ij} is given by (2.26), h^1_{ij} and h^2_{ijk} are solutions to the set of canonical variational problems (2.18) and (2.19), p^r_{ijk} are the associated adjoint states, solutions of the following set of variational problems:

$$p^k_{pqr} \in \mathcal{V} \ : \ \int_{\mathcal{Y}} \sigma(p^k_{pqr}) \cdot \varepsilon(\eta) = \int_{\mathcal{Y}} (\sigma(\tilde{\tilde{u}}_{pqr}) + \mathrm{C}(\tilde{u}_{pq} \otimes_s \mathrm{e}_r)) \cdot (\eta \otimes_s \mathrm{e}_k) - \int_{\mathcal{Y}} \mathrm{C}(\tilde{\tilde{u}}_{pqr} \otimes_s \mathrm{e}_k) \cdot \varepsilon(\eta) - \int_{\mathcal{Y}} \langle \sigma(\tilde{\tilde{u}}_{pqr}) + \mathrm{C}(\tilde{u}_{pq} \otimes_s \mathrm{e}_r) \rangle \cdot (\eta \otimes_s \mathrm{e}_k), \quad \forall \eta \in \mathcal{W}. \quad (3.12)$$

Here, $\mathbb{P}$ is the polarization tensor defined as

$$\mathbb{P} = -\frac{1-\gamma}{1+\gamma\beta}\left((1+\beta)\mathbb{I} + \frac{1}{2}(\alpha-\beta)\frac{1-\gamma}{1+\gamma\alpha}\mathrm{I}\otimes\mathrm{I}\right), \tag{3.13}$$

where I and $\mathbb{I}$ are defined in (2.3) and (2.4), and the parameters α and β given by

$$\alpha = \frac{\lambda+\mu}{\mu} \quad \text{and} \quad \beta = \frac{\lambda+3\mu}{\lambda+\mu}. \tag{3.14}$$

With the topological derivatives of the homogenized tensors C^h and D^h, an optimization procedure can now be set up.

4. Gradient type method for topological optimization

In a general manner, we consider the following minimization problem:

$$\inf_{\Omega}\left\{\mathcal{J}(\Omega) := j(\mathrm{C}^h(\Omega), \mathrm{D}^h(\Omega))\right\}, \tag{4.1}$$

where Ω is the stiff part of the unit cell $\mathcal{Y}$ defined in Section 2, and the shape functional $\mathcal{J}$ is defined from a smooth real-valued map j depending on the homogenized tensors.

4.1. **The algorithm.**

To solve problem (4.1), we use a gradient-type method based on the topological derivative, which was introduced in (Amstutz and Andrä, 2006), and used in (Amstutz et al., 2010) to tackle optimization problems of functionals depending only on C^h.

4.1.1. *Outline of the algorithm.* For a complete description of the algorithm, we refer to the pioneering papers (Amstutz and Andrä, 2006; Amstutz, 2011). The basic idea is to make use of the topological derivative as a steepest-descent direction, analogously to the methods using the gradient of the cost function in classical optimization. Here we consider, as in Section 3.1, the case where the perturbation of the domain is performed by either the inclusion of a small circular set of material **(a)** into the material **(b)**, or the inclusion of a small circular set of material **(b)** into the material **(a)**. Thus we want to use the following topological asymptotic expansion to implement an optimization procedure:

$$\mathcal{J}(\Omega_{\rho,\hat{y}}) = \mathcal{J}(\Omega) + g(\rho)D_T\mathcal{J}(\Omega)(\hat{y}) + o(g(\rho)). \tag{4.2}$$

This expansion delivers the following necessary local minimality condition for the problem (4.1) under the class of domain perturbations depicted above, which is

$$D_T\mathcal{J}(\Omega)(\hat{y}) \geq 0, \quad \forall \hat{y} \in \Omega \cup (\mathcal{Y}\setminus\overline{\Omega}). \tag{4.3}$$

To take advantage of the optimality condition (4.3), we start representing the distribution of material composing the cell with a level-set function ψ. Namely we have

$$\Omega = \{x \in \mathcal{Y} \mid \psi(x) < 0\}, \tag{4.4}$$

$$\mathcal{Y}\setminus\overline{\Omega} = \{x \in \mathcal{Y} \mid \psi(x) > 0\}, \tag{4.5}$$

$$\Gamma = \{x \in \mathcal{Y} \mid \psi(x) = 0\}. \tag{4.6}$$

Now the idea is somehow to let the topological derivative $D_T\mathcal{J}(\Omega)$ plays the role of a "target level-set". Indeed, by defining a new signed topological derivative g_Ω^T as follows

$$g_\Omega^T(\hat{y}) = \begin{cases} -\,D_T\mathcal{J}(\Omega)(\hat{y}) & \text{if } \hat{y} \in \Omega, \\ +\,D_T\mathcal{J}(\Omega)(\hat{y}) & \text{if } \hat{y} \in \mathcal{Y}\setminus\overline{\Omega}, \end{cases} \tag{4.7}$$

we can rewrite the optimality condition (4.3) as being equivalent to the collinearity between the level-set ψ and the signed topological derivative g_Ω^T. Thus the optimality condition becomes

$$\exists \mathrm{c} > 0, \quad \psi = \mathrm{c}g_\Omega^T. \tag{4.8}$$

The distribution defined by the level-set ψ remains unchanged when we multiply it by a positive scalar. We can therefore normalize in L^2 norm both ψ and g_Ω^T without changing the procedure.

From now we consider that $\|\psi\|_{L^2(\mathcal{Y})} = 1$ and $\|g_\Omega^T\|_{L^2(\mathcal{Y})} = 1$. In order to control and drive the collinearity between this two fields, we choose to use θ the non orienting angle between them

$$\theta = \arccos(\langle g_\Omega^T, \psi \rangle_{L^2(\mathcal{Y})}). \tag{4.9}$$

For achieving the optimality condition, we make the level-set evolve "in the direction" of the topological derivative by rotating it of an angle $\kappa\theta$ in the plane $\text{span}\{\psi, g_\Omega^T\}$, where $\kappa \in [0, 1]$ plays the role of a step size. We denote by $C_{\kappa,\theta}(\psi)$ the result of this rotation, which is a linear combination of ψ and g_Ω^T given by (see (Amstutz and Andrä, 2006))

$$C_{\kappa,\theta}(\psi) = \frac{1}{\sin\theta}\left(\sin((1-\kappa)\theta)\psi + \sin(\kappa\theta) g_\Omega^T\right). \tag{4.10}$$

Thus the evolution of the level-set will follow the fixed point procedure $\psi = C_{\kappa,\theta}(\psi)$. The procedure is summarized in the following steps (see (Amstutz, 2011) for more details):

- Choose a initial level-set ψ_0 and an initial step size κ_0
- While the optimality condition (4.8) is not satisfied: iterate on $n \geq 0$
  - calculate the associated topological derivative g_n^T
  - update the level-set function within a line search

$$\psi_{n+1} = C_{\kappa_n,\theta_n}(\psi_n). \tag{4.11}$$

The step size κ_n is adapted in order to make sure that the level-set follows a descent direction: $\mathcal{J}(\Omega_{n+1}) < \mathcal{J}(\Omega_n)$, where $\Omega_{n+1} := \{\psi_{n+1} < 0\}$. Thus, the step size is decreased if the criterion is not improved.

We recall that our topological optimization problem depends on the homogenized tensors, for which we gave explicit formulas of the topological derivatives, and we made in the previous section the assumption that j in (4.1) is smooth. Thus we directly have the exact topological derivative of the shape functional $\mathcal{J}$ given by the chain rule

$$D_T\mathcal{J}(\Omega) = \left\langle D_1 j, D_T \mathrm{C}_\Omega^h \right\rangle + \left\langle D_2 j, D_T \mathrm{D}_\Omega^h \right\rangle. \tag{4.12}$$

4.1.2. *Numerical computation of the topological derivatives.* As we saw in the previous sections, in order to calculate the homogenized tensors and the topological derivatives of the homogenized tensors, we need to solve auxiliary boundary value problems defined on the cell, giving the first and second order correctors and the adjoint-sates.

We solve these problems and implement the optimization procedure in a *Matlab* code, for a computation of the fields by a Finite Element (FE) discretization. This code was implemented for the first-order homogenization and optimization of C^h in (Amstutz et al., 2010). For the present article, we have added the higher-order homogenization scheme, in order to compute the higher-order homogenization tensor, together with its topological derivative.

The design variable is the level-set ψ. For the discretization, we select a mesh $\mathcal{M}_h$, and we use P_1 elements. The numerical level-set ψ is defined by its nodal values. From this we define the field γ characterizing the distribution setting $\gamma = 1$ on the nodes for which the level-set $\psi < 0$, and $\gamma = \gamma_0$ on the nodes where $\psi \geq 0$. At this stage, the contrast field γ is defined by its nodal values. Then by linear interpolation from the nodes to the centers of the triangles, we calculate a contrast field which is constant on each triangle. The periodic boundary conditions imposed for the vector fields is ensured by a procedure described in (Giusti et al., 2009a). The solutions of approximated auxiliary problems (i.e. correctors and adjoint states) are computed and take their values on the nodes, while their gradients are constant on each triangular element. The homogenized tensors and their topological derivatives depend on the contrast field, and both on the correctors and adjoint states and their gradients. Thus we also interpolate the correctors and adjoint states from the nodes to the center of the triangular elements.

4.2. **Settings of the numerical study.** The sequence of domains $(\Omega_n)_{n\geq 0}$ produced by the optimization process are defined by $\Omega_n = \{\psi_n < 0\}$ and $\mathcal{Y} \setminus \overline{\Omega_n} = \{\psi_n > 0\}$, where ψ_n is the level-set at the step n, and where the cell is the unit square

$$\mathcal{Y} := (0,1) \times (0,1). \tag{4.13}$$

Both domains are characterized by the same Poisson coefficient

$$\nu := 0.3 \tag{4.14}$$

and by Young's moduli which differ from a contrast $\gamma_0 = 0.01$, that is

$$E_{\{\psi<0\}} = 1, \tag{4.15}$$

$$E_{\{\psi>0\}} = 0.01. \tag{4.16}$$

Except when specified, the initial step size κ_0 is taken equal to 1, and the initial distribution $\Gamma_0 = \{x \in \mathcal{Y} \mid \psi_0(x) = 0\}$ that we consider is a disk (see Figure 3).

The procedure is sensitive to the initialization. It depends both on the size of the mesh and on the initial shape Γ_0, and can converge to different local solutions. Indeed the minimization problems we tackle numerically are not well-posed. They can have several local minima, and may not even have global minimum. However we will see in Section 5.2.1 that algorithm encounters a form of stability with respect to the initial data. We start with a rather coarse mesh, so that we can reach rapidly but not precisely a local minimum, and then we refine the mesh. The mesh we choose is made with structured triangles (see Figure 3). We divide the cell $\mathcal{Y}$ with n_i^2 squares crossed by their diagonals, giving $4n_i^2$ triangles elements. When a *homogeneous refinement* is performed, each triangle element is subdivided into four triangle elements of the same area. When a *local refinement* is performed, only the elements on which the topological derivative is high are subdivided, and the threshold is empirically set at 75% of the maximum value of the topological derivative. Now we present in the following and last section the optimization problems we have investigated.

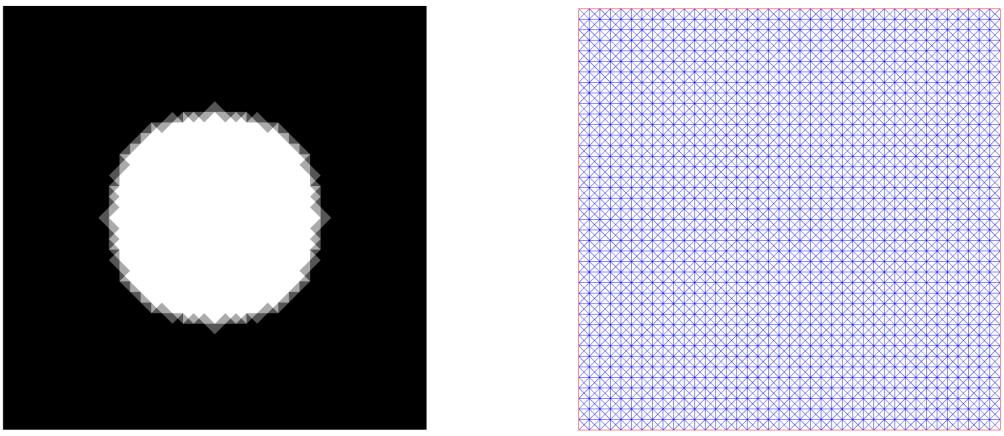

FIGURE 3. Initial black (stiff material) and white (soft material) distribution on the left, and initial mesh on the right, both given for a number of squares $n_i = 40$ along one side of $\mathcal{Y}$.

5. Optimized microstructures

After having made a state of the art of the results we need, we now present their application to the synthesis of microstructures featuring strain-gradient effects. We start by defining in Section 5.1 the characteristic lengths on which relies the optimization procedure. Then different

shape functionals are investigated in Sections 5.2 to 5.4, as well as a study of the convergence and the sensitivity to the initialization of the optimization procedure. Finally, the optimized microstructures are evaluated for a large material property contrast in Section 5.5.

5.1. **Strain-gradient characteristic lengths.** A second-gradient model having a macroscopic strain energy given by (2.28) contains some intrinsic characteristic lengths. Indeed, by considering a strain tensor E, and a vector $e \in \mathbb{R}^2$, we can define an intrinsic characteristic lengths as follows:

$$l_{E,e} = \sqrt{\frac{(E \otimes e) \cdot \mathrm{D}^h (E \otimes e)}{E \cdot \mathrm{C}^h E}}, \tag{5.1}$$

which can be interpreted as a measure of the sensitivity of the material to a variation of the strain E in the direction e: $K = E \otimes e$. If a microstructure leads to a strain-gradient homogenized model, then the characteristic length measures the relative weight of C^h and D^h in the energy.

We consider the unit strains of uniaxial extension $E^{11} = \mathrm{e}_1 \otimes \mathrm{e}_1$, and $E^{22} = \mathrm{e}_2 \otimes \mathrm{e}_2$, and of pure shear $E^{12} = \mathrm{e}_1 \otimes_s \mathrm{e}_2$, and their variations in the directions e_1 and e_2. This gives the following definition of the six different arising characteristic lengths:

$$\begin{aligned} l_{111} &= \sqrt{\frac{\mathrm{D}^h_{111111}}{\mathrm{C}^h_{1111}}}, \quad l_{221} = \sqrt{\frac{\mathrm{D}^h_{221221}}{\mathrm{C}^h_{2222}}}, \quad l_{121} = \sqrt{\frac{\mathrm{D}^h_{121121}}{\mathrm{C}^h_{1212}}}, \\ l_{112} &= \sqrt{\frac{\mathrm{D}^h_{112112}}{\mathrm{C}^h_{1111}}}, \quad l_{222} = \sqrt{\frac{\mathrm{D}^h_{222222}}{\mathrm{C}^h_{2222}}}, \quad l_{122} = \sqrt{\frac{\mathrm{D}^h_{122122}}{\mathrm{C}^h_{1212}}}. \end{aligned} \tag{5.2}$$

From this, we intend to maximize these characteristic lengths. Indeed, by maximizing these ratios, we force some components of the tensor C^h to be small, and even close to zero. In this case we obtain some zero strain energy modes, also called *floppy modes* (Durand et al., 2022), corresponding to this apparition of a kernel for C^h. Then, for strains belonging to this kernel, the strain-gradient elastic energy weighted by τ^2 and depending on D^h becomes more significant than the classical first-gradient energy depending on C^h in the energy (2.28). Namely, we numerically maximize the strain-gradient energy while minimizing the first-gradient energy relatively to some strain modes.

It is worth to note that in the case of a centrosymmetric unit cell, the odd order coupling tensor E^h between E and K vanishes (see (Smyshlyaev and Cherednichenko, 2000)). As we choose centrosymmetric initial unit cells, it turns out that the optimized unit cells we obtain are also centrosymmetric, even if nothing enforces this symmetry.

In addition, we want to observe the effects of a gradient of deformation throughout several cells. It means that the characteristic lengths need to be of order of several cells, or at least one cell. Indeed, in the expression of the energy, D^h is multiplied by τ^2, and then the characteristic lengths deriving from the energy are given by τl_{ijk}. In view of the definition of the cell in (4.13), we wish to have l_{ijk} greater than 1.

In view of the isotropic initial distribution and the square shape of the unit cell (see Figure 3), we first only consider the maximization of l_{111}, l_{112}, and l_{121}, because from a square unit cell, we obtain the same results rotated with a $\pi/2$ angle by respectively maximizing l_{222}, l_{221}, and l_{122}.

Before numerical investigation, we give the values of these characteristic lengths for the initial cell defined in Figure 3, and for a mesh $n_i = 100$:

$$l_{111} \simeq i\, 0.3655, \tag{5.3}$$

$$l_{112} \simeq i\, 0.0926, \tag{5.4}$$

$$l_{121} \simeq i\, 0.0933, \tag{5.5}$$

noting that in each case the lengths are imaginary, because the coefficients D^h_{111111}, D^h_{112112}, and D^h_{121121} are negative. In the following, we are going to maximize the square of these lengths,

and we will observe that for each optimized shape that we obtain, the coefficients of D^h will be positive, and thus the optimized lengths will be real lengths. Indeed, it is observed in (Durand et al., 2022) that for zero strain energy mode – that we are creating by maximizing the associated characteristic length –, the corresponding part of D^h turns to be positive.

5.2. **The horizontal elongation.** In (Alibert et al., 2003; Seppecher et al., 2011), the authors study a pantographic beam made of crossed rods connected via perfect junctions. This structure features an extensional floppy mode for a deformation E^{11} and a non zero energy for a gradient in the horizontal deformation K^{111}. This can be seen as $\mathrm{C}^h_{1111} = 0$ and $\mathrm{D}^h_{111111} > 0$ for the homogenized tensors of the structure. We would like to retrieve this strain-gradient behavior in the framework of continuous materials. Thus, we minimize the functional:

$$j(\mathrm{C}^h, \mathrm{D}^h) = -\frac{\mathrm{D}^h_{111111}}{\mathrm{C}^h_{1111}}. \tag{5.6}$$

The mesh is initialized with $n_i = 100$. We have made two local refinements of the mesh at the iterations 20 and 26, before the level-set finally reached an optimum for a total of 29 iterations, with an angle $\theta \simeq 9.30°$ Surprisingly, in view of the simplicity of the functional involved, we obtain in Figure 4 a pantographic like cell (see e.g., (Seppecher et al., 2011; Milton, 2013; McMahan et al., 2022)). Here are the value of the component of interest for the final distribution:

$$\mathrm{C}^h_{1111} \simeq 0.1079, \tag{5.7}$$

$$\mathrm{D}^h_{111111} \simeq 0.0183., \tag{5.8}$$

that is

$$l_{111} \simeq 0.4114. \tag{5.9}$$

We can see that the junctions allows a small relative rotation of the stiff parts. For homogeneous deformation E^{11}, the rotations of all the stiff parts are compatible, and we can see on Figure 4 that the structure can extend because of these rotations (the South and North inner junctions are moving away while the East and West junctions are moving closer together). But for a gradient of deformation $K^{111} = \mathrm{e}_1 \otimes \mathrm{e}_1 \otimes \mathrm{e}_1$, the rotations are incompatible, so that this macroscopic deformation mode costs in energy.

In Figure 4, we also present three total displacement fields of the unit cell, when this latter is subjected either to an homogeneous strain deformation E^{11}, or to a homogeneous strain-gradient deformations K^{111}, or $K^{112} = \mathrm{e}_1 \otimes_s \mathrm{e}_1 \otimes \mathrm{e}_2$. These deformation modes are derived from the expansion (2.17) by choosing a suitable U, so that respectively $\nabla^s U(y) = \mathrm{e}_1 \otimes_s \mathrm{e}_1$, $\nabla\nabla^s U(y) = \mathrm{e}_1 \otimes_s \mathrm{e}_1 \otimes \mathrm{e}_1$, and $\nabla\nabla^s U(y) = \mathrm{e}_1 \otimes_s \mathrm{e}_1 \otimes \mathrm{e}_2$. Thus, the corresponding total displacement fields obtained can be respectively given by

$$u^{11}(y) = y_1 \mathrm{e}_1 + h^1_{11}(y), \tag{5.10}$$

$$u^{111}(y) = \frac{1}{2} y_1^2 \mathrm{e}_1 + h^1_{11}(y) y_1 + h^2_{111}(y), \tag{5.11}$$

$$u^{112}(y) = y_1 y_2 \mathrm{e}_1 - \frac{1}{2} y_1^2 \mathrm{e}_2 + h^1_{11}(y) y_2 + h^2_{112}(y). \tag{5.12}$$

For each of these deformation modes, the local norm of the corresponding stress fields $\|\sigma\| := (\Sigma^2_{i,j=1} \sigma^2_{ij})^{1/2}$ is represented in logarithmic scale only in the stiff material, and the deformed geometry is displayed with a scale factor for readability.

Before exploring more functionals, we present the behavior of the optimization procedure with respect to the initialization, the choice of the cell and the mesh convergence.

5.2.1. *Sensitivity to the initial guess and mesh.* First we investigate the effect of the initial level-set and of the initial mesh on the convergence of the algorithm. For this we consider the problem of minimization of the functional defined in (5.6), for several perturbations of the initial level-set in Figure 3. For all i in $\{-4, -3, \cdots, 3, 4\}$ we consider the new initial level-set functions

$$\psi_{0,i} := \psi_0 + 0.05i. \tag{5.13}$$

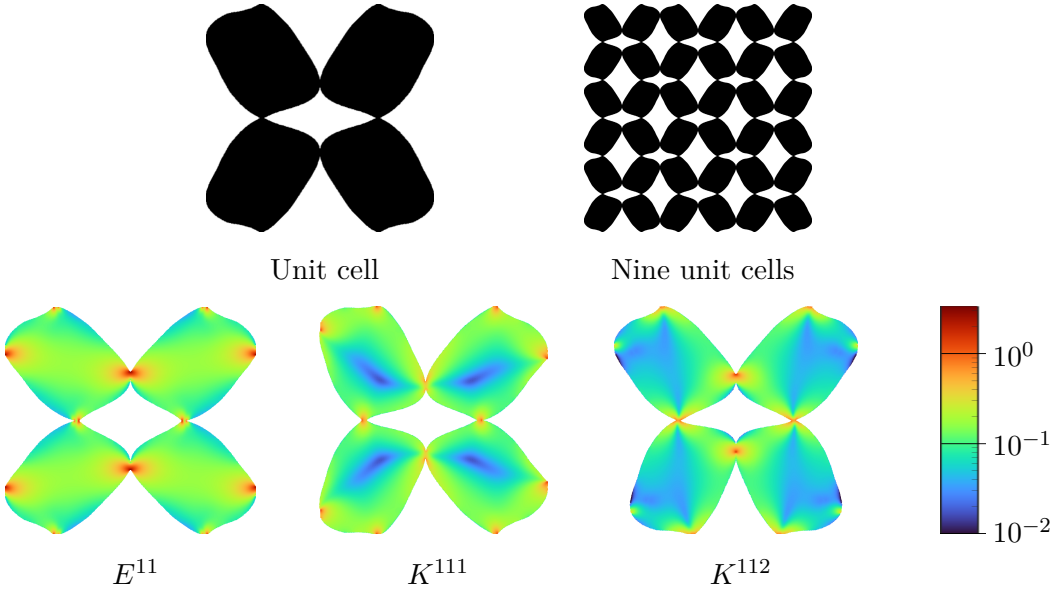

FIGURE 4. Results for the minimization of the cost function (5.6): maximization of the characteristic length l_{111}. From left to right: optimum unit cell; periodic microstructure; deformed geometry for the deformation modes E^{11}, K^{111}, and K^{112}, together with the corresponding local stress norm in logarithmic scale.

At the same time we also consider, for each of these initial level-set functions, different initial meshes. Namely n_i varies in $\{40, 60, 80, 100, 120, 140\}$. The final resulting distributions are gathered in Figure 5.

As expected, the optimization procedure is sensitive to initial data, and both the initial level-set and the initial mesh influence the final result. Nevertheless, Figure 5 shows some characteristic patterns in the optimized results. In fact we observe that several optimized distributions do look like *pantographic* material (see Figure 4) such as results $(15-18)$, $(21-24)$, $(27, 28)$, (42). The result (1) has got also a lot of similar results (sometimes translated half a unit-cell): $(3-11)$, $(13-14)$, (19), (25), $(29, 30)$, $(33, 34)$, (38), $(40, 41)$, $(45-47)$, and $(52-54)$. This indicates a kind of stability of the topological optimization procedure for the present functional.

Furthermore, even by changing the initial shape of the distribution (but with the same initial topology) the algorithm produces similar results. For example, still within the maximization of l_{111}, we consider an initial rectangular inclusion of material (see Figure 6 (d)). The final level-set obtained Figure 6 is quite similar to the result (1) from Figure 5. Finally, the microstructures having the best characteristic length l_{111} are actually the pantographic cells, such as the one we obtained in Figure 4.

5.2.2. *Position and number of unit cells.* It is known that the periodic solutions to the variational problems (2.18) and (2.19) remain unchanged up to a translation when the distribution of material is translated in the unit cell, or when the cell is redefined as the union of several unit cells. Then, from definitions (2.29) and (2.30), the homogenized tensors remain unchanged under such transformations. To observe this property, we consider the unit cells (a), (b) and (c) from Figure 6, with meshes defined by $n_i = 50$ for (a) and (c), and $n_i = 100$ for (b). From this we maximize the length l_{111}. For all the cases (a), (b), and (c), we perform a homogeneous refinement of the mesh at iteration 27, and the final topologies are obtained after a total of 37 iterations, for an final angle $\theta \simeq 5.88°$ every time. The results are presented Figure 6, and show that the topological optimization procedure does not depend on the choice of the cell.

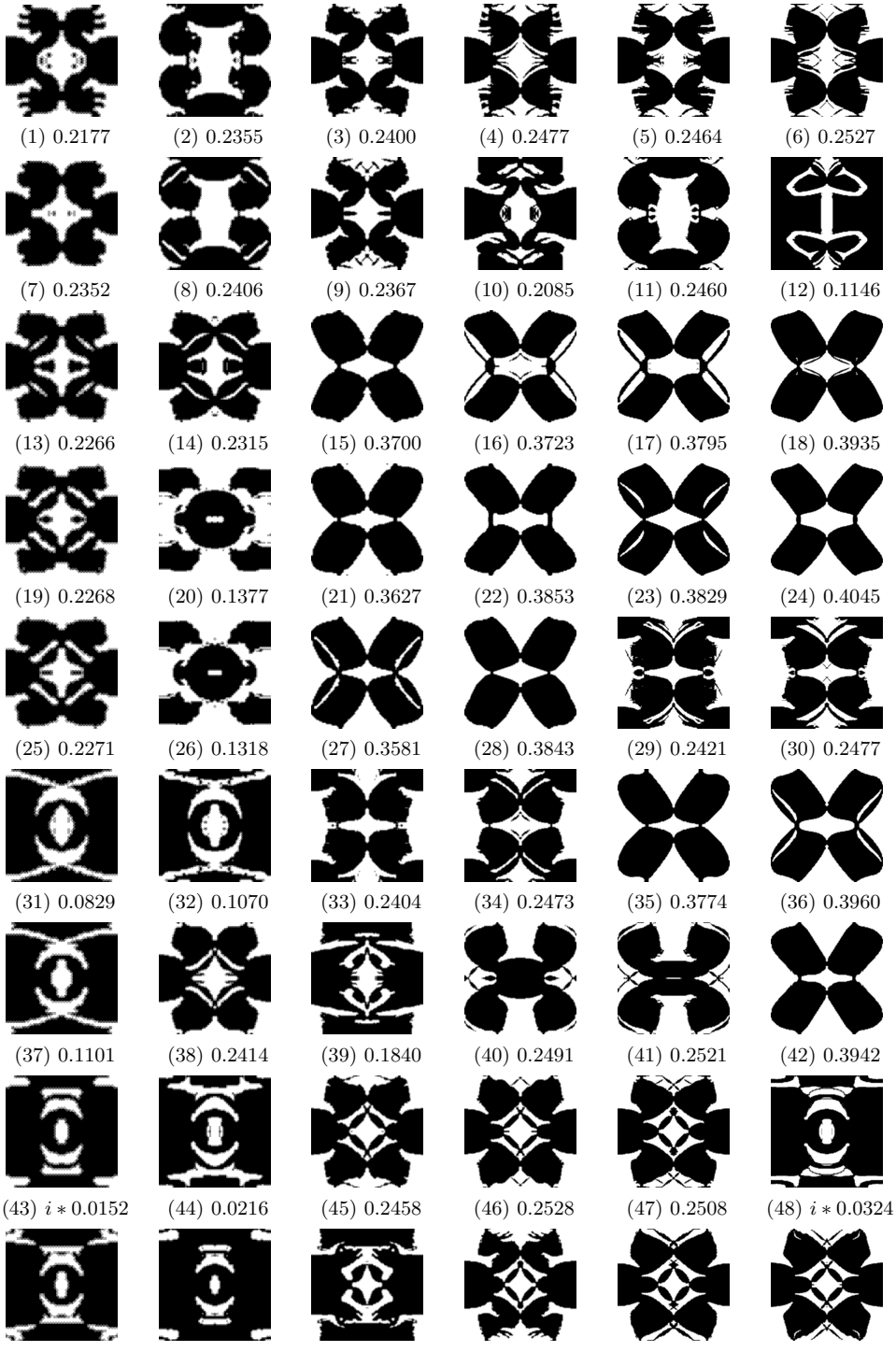

FIGURE 5. Different final level-sets and their corresponding characteristic lengths l_{111} obtained when the initial level-set and the size of the initial mesh vary. Each line from the top to the bottom is obtained for the level-sets from $\psi_{0,-4}$ to $\psi_{0,4}$ defined in (5.13). Each column corresponds to different mesh sizes.

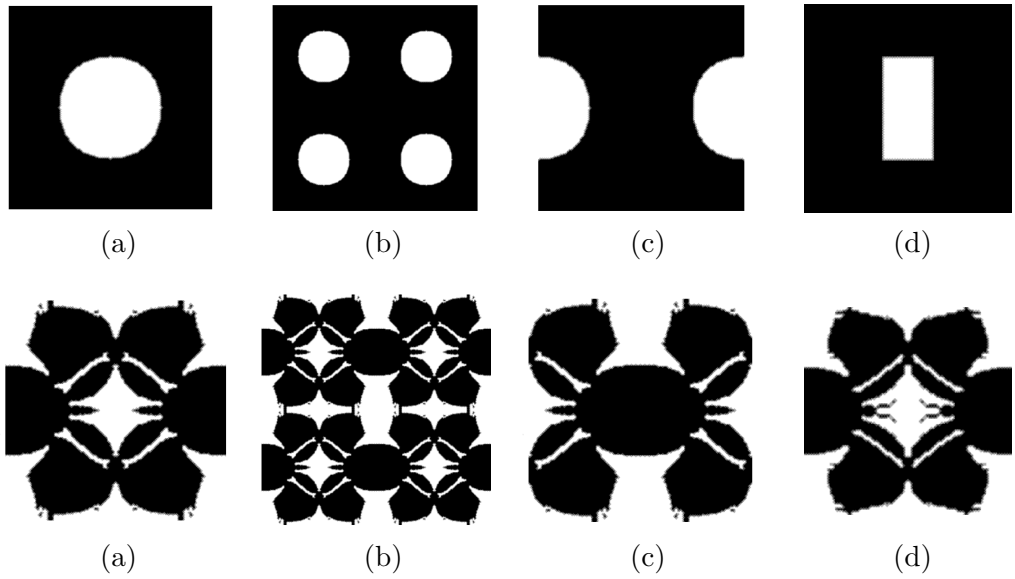

FIGURE 6. Maximization of the characteristic length l_{111}. From left to right: initial distribution; optimized distribution. From left to right: (a) $ni = 100$, $\mathcal{Y}_{\rm a} = (0,1) \times (0,1)$. (b) $ni = 200$, $\mathcal{Y}_{\rm b} = (0,2) \times (0,2)$. (c) $ni = 100$, $\mathcal{Y}_{\rm c} = (0.5,1.5) \times (0,1)$. (d) $ni = 100$, $\mathcal{Y}_{\rm d} = (0,1) \times (0,1)$.

5.2.3. *Mesh convergence.* Finally we investigate the algorithm convergence with respect to the mesh. We have seen in the previous paragraphs that the size of the initial mesh can affects the final result, and leads the algorithm to reach a local optimum rather than another. In order to analyse it, we go back to the initial circular level-set, and for an initial mesh characterized by $n_i = 100$. The algorithm converges to the solution that we display once again in Figure 7 (i), for a final angle $\theta \simeq 18.54°$. After the algorithm reached the state (i), we perform a homogeneous refinement of the mesh leading to Figure 7 (ii) for a final angle $\theta \simeq 10.18°$. We repeat the refinements one more time resulting in (iii) for an angle $\theta \simeq 9.08°$.

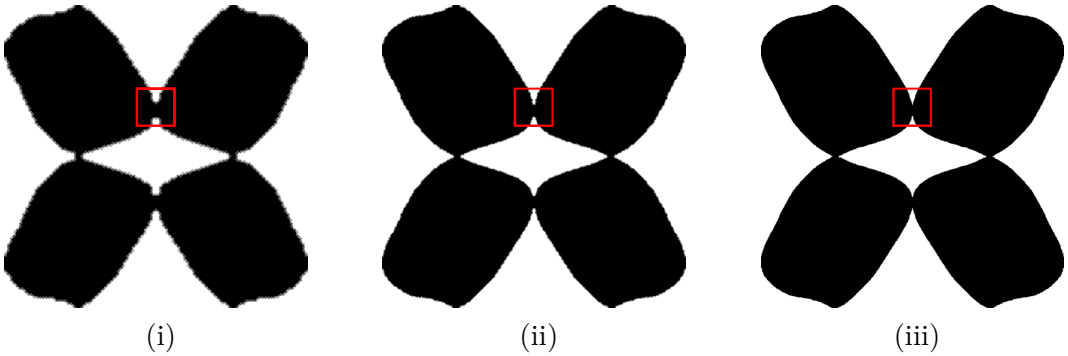

FIGURE 7. Final optimum topologies for the maximization of l_{111}, initial circular level-set, $n_i = 100$. (i) no refinement of the mesh. (ii) one refinement of the mesh. (iii) two refinements of the mesh.

Junction regions surrounded by the red rectangles in Figure 7, are displayed with a zoom in Figure 8. We measure the thinnest width between two nodes of black elements in the horizontal junction. The width is $\simeq 0.04$ for (i), $\simeq 0.035$ for (ii), and $\simeq 0.0325$ for (iii). Hence, it seems that the width of this junction is stable when the mesh size goes to zero. Indeed, the small

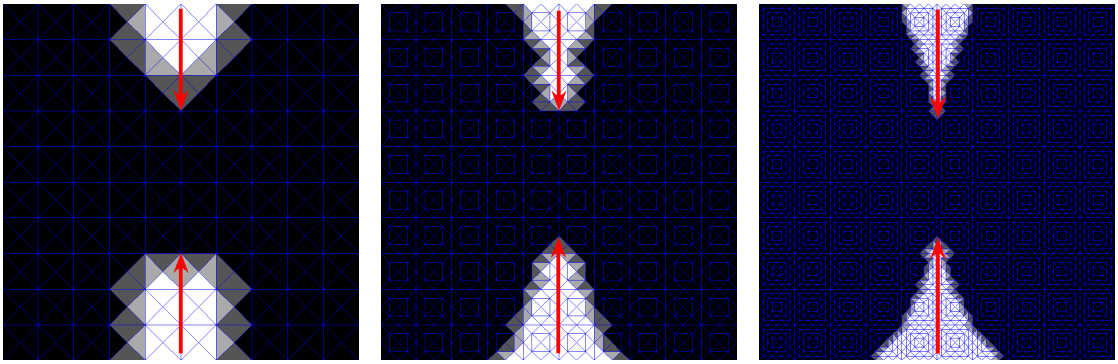

(i) (ii) (iii)

FIGURE 8. Zoom on the junctions surrounded by red rectangles from Figure 7. The new frame is $(0.45, 0.55) \times (0.6, 0.7)$.

decrease between (i) and (iii) is specific to the resolution: the fineness of the mesh making the measure more accurate.

Let us recall that, this kind of optimization procedure does not always converge with the mesh without a regularization of the optimization problem, such as perimeter or Von-Mises stress constraints. Such regularizations are often used in numerical procedures, and are generally necessary to show the theoretical existence of an optimum. In order to ensure the existence of an optimal domain to (1.1) e.g., the regularization by perimeter of Ω could be used in a proper way (Amstutz and Van Goethem, 2012). Nevertheless, we emphasize that in the present study we did not use any regularization.

5.2.4. *Length:* l_{112}. We are now interested in the effects of the gradient of the horizontal elongation in direction e_2: K^{112}. In this case, we minimize the following functional:

$$j(C^h, D^h) := -\frac{D^h_{112112}}{C^h_{1111}}. \tag{5.14}$$

The mesh is initialized with $n_i = 100$. After 18 iterations, the level-set reaches almost its final shape, for an angle $\theta \simeq 8.15°$. Then we perform a local refinement of the mesh, and we obtain the final distribution for a total number of iterations of 27, and a final angle $\theta \simeq 5.33°$. Here are the values of the component of interest for the final distribution which is presented in Figure 9:

$$C^h_{1111} \simeq 0.0753, \tag{5.15}$$

$$D^h_{112112} \simeq 0.0034. \tag{5.16}$$

which corresponds to

$$l_{112} \simeq 0.2139. \tag{5.17}$$

The final distribution is made of stiff parts connected by rods. We notice that the deformation mode K^{112} results in high stress levels in comparison to K^{111}. This latter deformation mode can be seen as a bending of the unit cell, which is restrainde by the incompatible relative rotations of the stiff parts.

5.3. **The shear deformation.** Now we consider the pure shear deformation E^{12}, and maximize the gradient of pure shear deformation in the horizontal direction e_1, by means of the following functional:

$$j(C^h, D^h) := -\frac{D^h_{121121}}{C^h_{1212}}. \tag{5.18}$$

The mesh is initialized with $n_i = 100$. The optimum distribution is reached after 17 iterations for an angle $\theta \simeq 0.01°$ (see Figure 10). Here are the values of the component of interest for the

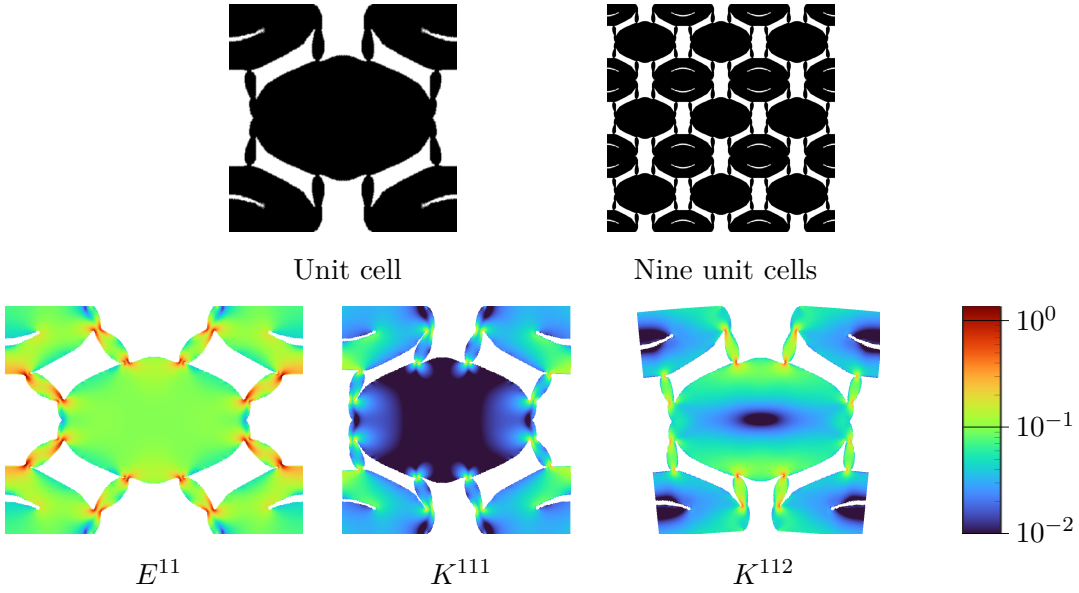

FIGURE 9. Results for the minimization of the cost function (5.14): maximization of the characteristic length l_{112}. From left to right: optimum unit cell; periodic microstructure; deformed geometry for the deformation modes E^{11}, K^{111}, and K^{112}, together with the corresponding local stress norm in logarithmic scale.

final distribution:

$$\mathrm{C}^h_{1212} \simeq 0.0250, \tag{5.19}$$

$$\mathrm{D}^h_{121121} \simeq 0.0522. \tag{5.20}$$

that is

$$l_{121} \simeq 1.4442. \tag{5.21}$$

It is interesting to observe that we obtain a laminated cell. Indeed, it was shown in (Briane and Camar-Eddine, 2012) that under certain conditions on the asymptotic behavior of material contrast and the volume fraction, a second gradient term – the gradient of the rotation – is appearing in the limit energy of a periodic laminated elastic material, resulting in a Koiter model. The result we obtain seems quite stable: for a change in the initial parameters such as the fineness of the mesh, or for a change in the initial distribution of material, the optimization scheme still leads to a laminated cell. We can observe that the horizontal strip of soft material allows a shear deformation without costing much elastic energy. But the presence of the horizontal beams of stiff material withstands to a horizontal gradient of the shear deformation.

Now we consider the maximization of both characteristic lengths l_{121} and l_{122}, namely we minimize the following functional:

$$j(\mathrm{C}^h, \mathrm{D}^h) := -\frac{\mathrm{D}^h_{121121} + \mathrm{D}^h_{122122}}{\mathrm{C}^h_{1212}}. \tag{5.22}$$

The mesh is initialized with $n_i = 60$, and we take an initial step size $\kappa_0 = 0.75$. After a local refinement of the mesh, we obtain the final distribution presented on Figure 11 after 19 iterations, and the final angle is $\theta \simeq 13.16°$. As a result, we obtain the microstructure displayed in Figure 11 composed with stiff parts in the form of discs connected to each other by two rods, and the following lengths:

$$\sqrt{l^2_{121} + l^2_{122}} \simeq 0.7285, \quad \text{and} \quad l_{121} = l_{122} \simeq 0.5151. \tag{5.23}$$

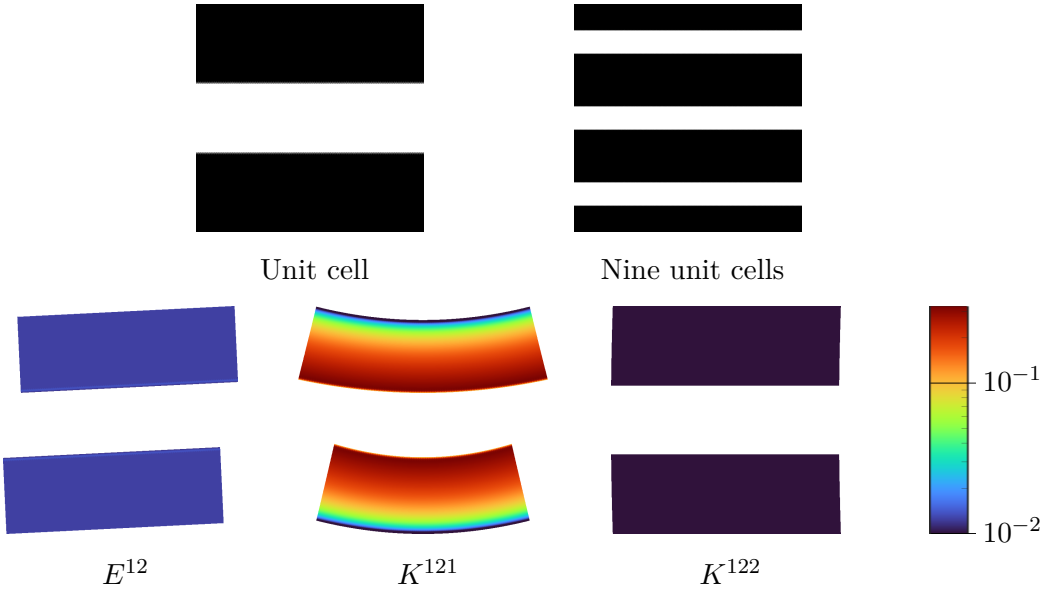

FIGURE 10. Results for the minimization of the cost function (5.18): maximization of the characteristic length l_{121}. From left to right: optimum unit cell; periodic microstructure; deformed geometry for deformation modes E^{12}; K^{121}, and K^{122}, together with the corresponding local stress norm in logarithmic scale.

We observe that shear deformations are facilitated by the presence of the connected rods which then start to rotate, and allow the stiff parts to move. In this case the stress is concentrated in the junction areas between the connecting rods and the stiff parts. But for a vertical or horizontal gradient of shear deformation, the connected rods are either stretched or compressed, and the stress propagate also in the stiff parts. In addition, we notice that the layout between the stiff parts and the connecting rods allows a small free rotation of the stiff parts.

5.4. **Pantographic-like microstructure.** A *pantographic continuous material* has been introduced and studied in (Durand et al., 2022). It corresponds to a 2-dimensional periodic material constituted with triangles and rhombuses being connected together via thin junctions (Figure 12). Their layout produces the behaviour of a pantographic-like material. This material first gradient elasticity features has floppy modes. One in extension E^{11}, and another one in shear E^{12}. Its macroscopic behaviour is described by a strain-gradient model. Surprisingly, we retrieve it through the topological optimization procedure.

For this we consider the rectangular unit cell

$$\mathcal{Y} = (0,1) \times (0,2). \tag{5.24}$$

In (Durand et al., 2022), the characteristic lengths of the pantograph for the unit cell $\mathcal{Y}$ have been evaluated, and l_{111} and l_{112} turn to have significant values. We consider the following functional to be minimized

$$j(\mathrm{C}^h, \mathrm{D}^h) = -\frac{\mathrm{D}^h_{111111} + \mathrm{D}^h_{112112}}{\mathrm{C}^h_{1111}}. \tag{5.25}$$

We choose an initial mesh for which the vertical direction of the rectangle is subdivided into $n_i = 120$ crossed squares, and the horizontal direction is subdivided into $n_i = 60$ crossed squares. The initial step size is $\kappa_i = 0.75$. Finally we choose an initial level-set function which results into shifted strips of holes (see Figure 13). After 29 iterations, we perform a homogeneous refinement of the mesh, followed by a local refinement of the mesh after 9 iterations. For a total of 45 iterations, the final angle is $\theta \simeq 5.35°$, and the optimized distribution is shown Figure 13.

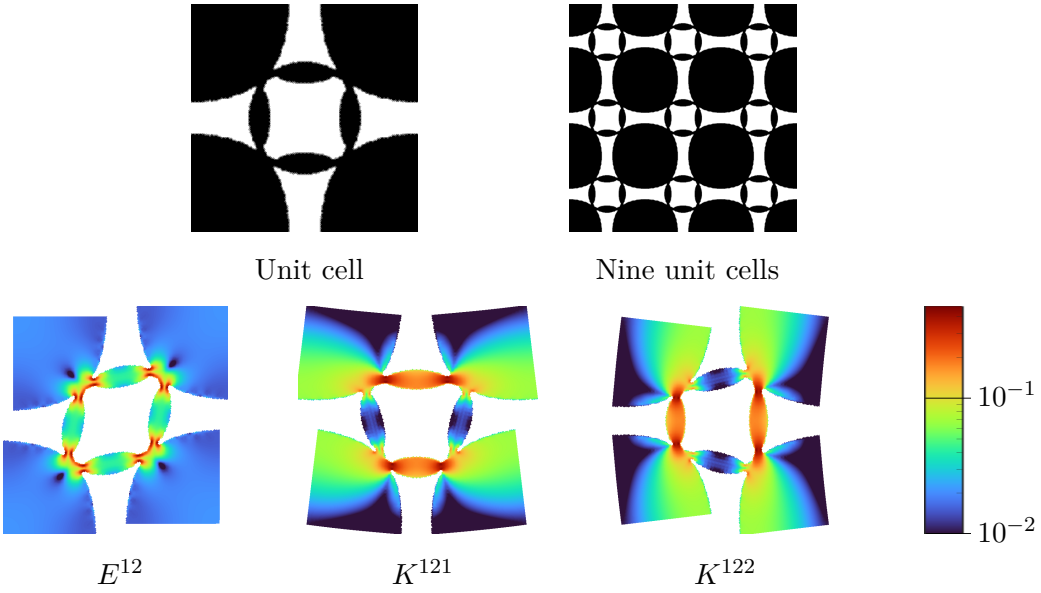

FIGURE 11. Results for the maximization of the cost function (5.22): maximization of the characteristic lengths l_{121} and l_{122}. From left to right: optimum unit cell; periodic microstructure; deformed geometry for the deformation modes E^{12}, K^{121}, and K^{122}, together with the corresponding local stress norm in logarithmic scale.

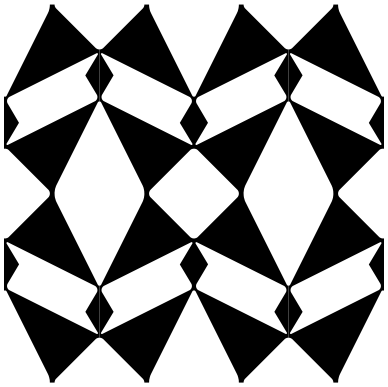

FIGURE 12. Pantograph (Figure from (Durand et al., 2022)).

We finally get

$$l_{111} \simeq 0.2548, \quad l_{112} \simeq 0.4578. \tag{5.26}$$

We can notice that the shape we get in Figure 13 looks very much like the pantograph from Figure 12, for which the triangles are smoothed, the rhombuses are replaced by more elliptic shapes, and some extra connecting rods are present.

5.5. **Very large contrast.** In the previous sections, we have obtained new interesting microstrucures by optimizing different strain-gradient effects. But the strain-gradient behaviour, which is quantified by the characteristic lengths we have introduced, is not very significant. Except in the case of the laminated cell, we have obtained characteristic lengths between 0.2 and 0.5 times the size of the unit cell. In comparison, the strain-gradient effects observed in (Durand et al., 2022) are more pronounced. This difference has two possible explanations. First, the computations led in (Durand et al., 2022) are made in the case where the cell is made up of a stiff material and voids, whereas in the present case, the cell is a mixture of a stiff and soft

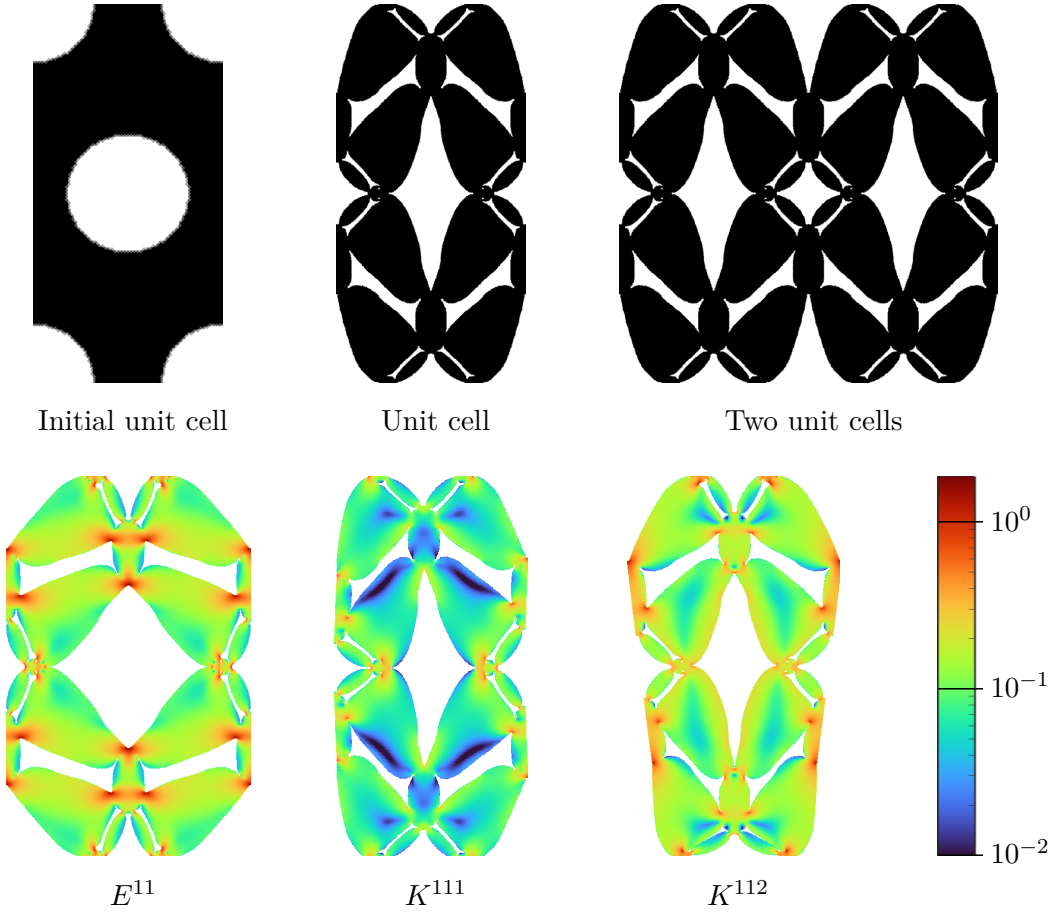

FIGURE 13. Results for the minimization of the cost function (5.25): maximization of the sum $l_{111} + l_{112}$. From left to right: initial unit cell; optimum unit cell; periodic microstructure; deformed geometry for the deformation modes E^{11}, K^{111}, and K^{112}, together with the corresponding local stress norm in logarithmic scale.

materials. Secondly, the junction regions of the pantograph in (Durand et al., 2022) are chosen arbitrarily thin, which brings on the strain-gradient behaviour.

Therefore, we investigate the characteristic lengths of the microstructures we have obtained, assuming the soft material is replaced by voids. We consider the level-set functions ψ obtained after the topological optimization for a contrast $\gamma_0 = 10^{-2}$, and for each of these geometries, we compute for a contrast $\gamma_0 = 10^{-8}$ the homogenized tensors C^h and D^h. For this, we need to change slightly the model for the higher order correctors h^2_{ijk}. Indeed we can see on equation (2.19) the presence of a body force depending on C^h which is applied homogeneously on the unit cell $\mathcal{Y}$. When the contrast γ_0 goes to zero, it means that a load is applied on the very weak material. We adopt the approach followed in (Durand et al., 2022). Let φ be the normalized characteristic function defined by

$$\varphi(y) := \frac{1}{\int_{\mathcal{Y}} \chi} |\mathcal{Y}| \chi(y), \tag{5.27}$$

where χ is the characteristic function of the stiff material, defined directly from the level-set ψ. The first auxiliary problem (3.3) remains unchanged, because it does not involve any body

force, while the second auxiliary problem (3.4) is replaced by

$$h^2_{ijk} \in \mathcal{V} \ : \ \int_{\mathcal{Y}} \sigma(h^2_{ijk}) \cdot \varepsilon(\eta) + \int_{\mathcal{Y}} \mathrm{C}(h^1_{ij} \otimes_s \mathrm{e}_k) \cdot \varepsilon(\eta) = \int_{\mathcal{Y}} (\sigma(u^\rho_{ij}) - \varphi \mathrm{C}^h_\rho(\mathrm{e}_i \otimes_s \mathrm{e}_j)) \cdot (\eta \otimes_s \mathrm{e}_k) \quad \forall \eta \in \mathcal{W}. \quad (5.28)$$

				
$\gamma_0 = 10^{-2}$	l_{111}	0.4114	0.1295	0.2548
	l_{112}	0.3166	0.2139	0.4578
	$\mathbf{C}^h$ eigenvectors	$\begin{bmatrix}-0.19\\-0.98\\0.00\end{bmatrix}\begin{bmatrix}-0.98\\0.19\\0.00\end{bmatrix}\begin{bmatrix}0.00\\0.00\\1.00\end{bmatrix}$	$\begin{bmatrix}-0.18\\-0.98\\0.00\end{bmatrix}\begin{bmatrix}-0.98\\0.18\\0.00\end{bmatrix}\begin{bmatrix}0.00\\0.00\\1.00\end{bmatrix}$	$\begin{bmatrix}-0.19\\-0.98\\0.00\end{bmatrix}\begin{bmatrix}-0.98\\0.19\\0.00\end{bmatrix}\begin{bmatrix}0.00\\0.00\\1.00\end{bmatrix}$
	$\mathbf{C}^h$ eigenvalues	$(0.2615, 0.1022, 0.0800)$	$(0.2596, 0.0694, 0.0433)$	$(0.3203, 0.0922, 0.1067)$
$\gamma_0 = 10^{-8}$	l_{111}	1.2607	0.1714	0.6415
	l_{112}	1.1039	0.5554	1.2656
	$\mathbf{C}^h$ eigenvectors	$\begin{bmatrix}1.00\\-0.03\\0.00\end{bmatrix}\begin{bmatrix}-0.03\\-1.00\\0.00\end{bmatrix}\begin{bmatrix}0.00\\0.00\\1.00\end{bmatrix}$	$\begin{bmatrix}-0.06\\-1.00\\0.00\end{bmatrix}\begin{bmatrix}-1.00\\0.06\\0.00\end{bmatrix}\begin{bmatrix}0.00\\0.00\\1.00\end{bmatrix}$	$\begin{bmatrix}1.00\\-0.06\\0.00\end{bmatrix}\begin{bmatrix}-0.06\\-1.00\\0.00\end{bmatrix}\begin{bmatrix}0.00\\0.00\\1.00\end{bmatrix}$
	$\mathbf{C}^h$ eigenvalues	$(0.0177, 0.2188, 0.0705)$	$(0.2032, 0.0103, 0.0099)$	$(0.0209, 0.2528, 0.0813)$

FIGURE 14. Homogenization results of the previously obtained microstructures with a property contrast $\gamma_0 = 10^{-2}$, and homogenization results for the same microstructures with a new property contrast $\gamma_0 = 10^{-8}$. (I)

			
$\gamma_0 = 10^{-2}$	l_{121}	1.4442	0.5151
	l_{122}	0.0099	0.5151
	$\mathbf{C}^h$ eigenvectors	$\begin{bmatrix}-1.00\\-0.02\\0.00\end{bmatrix}\begin{bmatrix}-0.02\\1.00\\0.00\end{bmatrix}\begin{bmatrix}0.00\\0.00\\1.00\end{bmatrix}$	$\begin{bmatrix}-0.71\\-0.71\\0.00\end{bmatrix}\begin{bmatrix}-0.71\\0.071\\0.00\end{bmatrix}\begin{bmatrix}0.00\\0.00\\1.00\end{bmatrix}$
	$\mathbf{C}^h$ eigenvalues	$(0.6998, 0.0356, 0.0125)$	$(0.2843, 0.2348, 0.0176)$
$\gamma_0 = 10^{-8}$	l_{121}	1472	1.3979
	l_{122}	9.2409	1.3979
	$\mathbf{C}^h$ eigenvectors	$\begin{bmatrix}-1.00\\0.00\\0.00\end{bmatrix}\begin{bmatrix}0.00\\1.00\\0.00\end{bmatrix}\begin{bmatrix}0.00\\0.00\\1.00\end{bmatrix}$	$\begin{bmatrix}-0.71\\-0.71\\0.00\end{bmatrix}\begin{bmatrix}-0.71\\0.071\\0.00\end{bmatrix}\begin{bmatrix}0.00\\0.00\\1.00\end{bmatrix}$
	$\mathbf{C}^h$ eigenvalues	$(0.6933, 4.10^{-8}, 1.10^{-8})$	$(0.2353, 0.2055, 0.0024)$

FIGURE 15. Homogenization results of the previously obtained microstructures with a property contrast $\gamma_0 = 10^{-2}$, and homogenization results for the same microstructures with a new property contrast $\gamma_0 = 10^{-8}$. (II)

Figures 14 and 15 present the values of the characteristic lengths or of the shape functionals, for each of the microstructures we have obtained, for both the finite contrast $\gamma_0 = 10^{-2}$

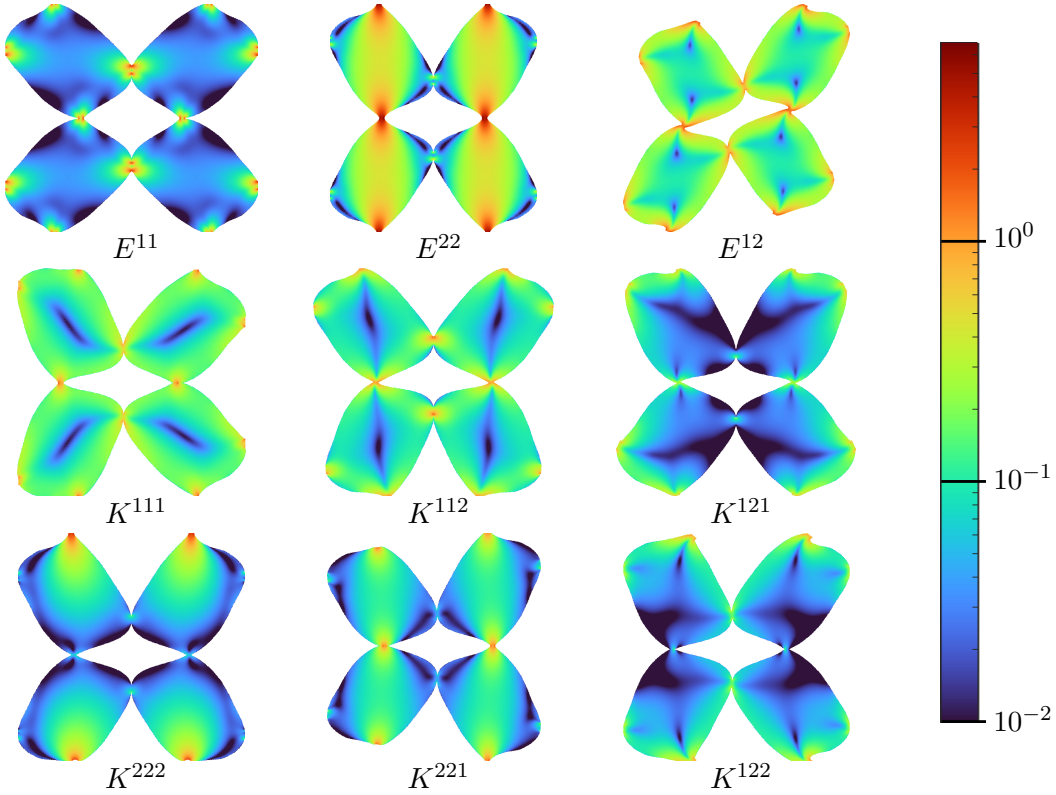

FIGURE 16. Deformed geometry of the pantographic cell obtained in Figure 4, for the deformation modes E^{ij} and K^{ijk} for $i, j, k = 1, 2$. The corresponding total displacement fields are computed in the case where the material contrast is $\gamma_0 = 10^{-8}$, and then the corresponding local stress norms are represented in logarithmic scale.

of the previous sections and the new very small contrast $\gamma_0 = 10^{-8}$. We observe that for each microstruture, considering this very small contrast improves significantly the characteristic lengths. For example for the two pantographic structures in Figure 14, the characteristic lengths are multiplied by a factor between 2.5 and 3.5.

Whereas, for a finite contrast $\gamma_0 = 10^{-2}$, C^h eigenvalues remain quite comparable, when the contrast is set to $\gamma_0 = 10^{-8}$ the expected floppy modes clearly emerge. For instance, in Figure 15 column 1, the eigenvalue related to E^{11} significantly drops from $\gamma_0 = 10^{-2}$ to $\gamma_0 = 10^{-8}$ whereas the other eigenvalues are not quite affected. This can be clearly observed in Figure 16, where we can see that E^{11} corresponds to a floppy mode in comparison to the other deformation modes E^{22} and E^{12}. We also observe in this figure that while the stress associated to the deformation mode E^{11} is not significant (and is obviously localized in the thin junctions), stress associated to the deformations modes K^{111} and K^{112} is more significant. Thus the obtained pantographic structure effectively displays strain gradient effects for deformations in the the direction e_1.

6. Conclusion

In the present article, we have numerically optimized strain-gradient effects for two-dimensional periodic material in elasto-statics. For this purpose, criteria depending on the homogenized tensors C^h and D^h are optimized, via an optimization method based on the topological derivatives of these homogenized tensors.

We have obtained non trivial microstructures for functionals based on intrinsic characteristic lengths. The latter are defined as a ratio of the coefficients of C^h and D^h. It is worth to notice that these microstructures are obtained by opening the kernel of C^h, so that the strain-gradient

terms depending on D^h become predominant in the macroscopic elastic energy. In particular, we have strikingly obtained well known microstructures featuring strain-gradient effects, such as a pantographic unit cell, similar to the one studied in (Durand et al., 2022). The convergence with respect to the mesh has been illustrated. Finally, the obtained microstructures has also been homogenized in the case of a large contrast between the stiff and the soft materials and strain-gradient effects were enhanced.

Note that, the homogenization scheme we used may also correctly predict second gradient effects in some situations where the material contrast is infinite (see (Durand et al., 2022)). Nevertheless, no general result of higher-order homogenization is known in this case (see (Briane and Camar-Eddine, 2012; Jakabčin and Seppecher, 2020)). Hence, the theoretical study of infinite contrast optimization of higher-order homogenization is also an open problem. As a consequence, it is not surprising that by optimizing second gradient effects defined by this finite contrast homogenization scheme, we could obtain microstructures corresponding to other homogenized models when the contrast is large. For example, the microsctructure obtained in Figure 11 can be compared with the square grid with isolated diagonals from (Jakabčin and Seppecher, 2020), case 3. In the referred article, it is numerically shown that a Cosserat model is the most accurate to describe this microstructure, in comparison to the first-gradient model and the second-gradient model, when the material contrast behaves as τ^3, with the size of the cell τ going to zero.

To go further in the optimization of strain-gradient effects, two different approaches that we will follow in future works are possible. The first one is to study functional depending on the invariants of the homogenized tensors. For C^h, these invariants are well-known. For D^h, there exists a very large number of invariants which were computed in (Auffray et al., 2021), and their mechanical understanding is still a subject of study. The second one is to consider functionals depending of the fifth-order tensor E^h of coupling moduli between first and second gradient effects. In the present study, we were not interested in this tensor because it cancels in the case of a centro-symmetric unit cell. But new microstructures could be explored by taking it into account.

Finally, we would like to point out that the case of dimension 3 could be treated in a similar way from a theoretical point of view, although the practical implementation of the optimization procedure as well as the large number of strain-gradient elastic moduli make this task much more complex.

Acknowledgements. The authors acknowledge the support of the French Agence Nationale de la Recherche (ANR), under grant ANR-17-CE08-0039 (project ArchiMatHOS). This work was partially funded by CNRS/IRP Coss&Vita between Fédération Francilienne de Mécanique (F2M, CNRS FR2609) and M&MoCS. V. Calisti has been supported by Praemium Academiæ of Š. Nečasová. The Institute of Mathematics, CAS is supported by RVO:67985840. The authors would also like to thank Pierre Seppecher for fruitful discussions.

References

H. Abdoul-Anziz, P. Seppecher, and C. Bellis. Homogenization of frame lattices leading to second gradient models coupling classical strain and strain-gradient terms. *Math. Mech. Solids*, 24 (12):3976–3999, 2019.

J.-J. Alibert, P. Seppecher, and F. Dell'Isola. Truss modular beams with deformation energy depending on higher displacement gradients. *Math. Mech. Solids*, 8(1):51–73, 2003.

G. Allaire. *Shape optimization by the homogenization method*, volume 146 of *Applied Mathematical Sciences*. Springer-Verlag, New York, 2002.

G. Allaire. *Conception optimale de structures*, volume 58 of *Mathématiques & Applications (Berlin) [Mathematics & Applications]*. Springer-Verlag, Berlin, 2007. With the collaboration of Marc Schoenauer (INRIA) in the writing of Chapter 8.

G. Allaire and T. Yamada. Optimization of dispersive coefficients in the homogenization of the wave equation in periodic structures. *Numerische Mathematik*, 140(2):265–326, 2018.

S. Amstutz. Analysis of a level set method for topology optimization. *Optimization Methods and Software*, 26(4-5):555–573, 2011.

S. Amstutz and H. Andrä. A new algorithm for topology optimization using a level-set method. *Journal of Computational Physics*, 216(2):573–588, 2006.

S. Amstutz and N. Van Goethem. Topology optimization methods with gradient-free perimeter approximation. *Inverse Problems and Imaging*, 14(3):401–430, 2012.

S. Amstutz, S. M. Giusti, A. A. Novotny, and E. A. de Souza Neto. Topological derivative for multi-scale linear elasticity models applied to the synthesis of microstructures. *International Journal for Numerical Methods in Engineering*, 84(6):733–756, 2010.

N. Auffray, B. Desmorat, and H. Abdoul-Anziz. Invariants of the 6th-order strain gradient elasticity tensor. *submitted*, 2021.

M. P. Bendsøe and O. Sigmund. *Topology optimization. Theory, methods and applications.* Springer-Verlag, Berlin, 2003.

M. Bendsøe. Optimal shape design as a material distribution problem. structural optimization 1, 193-202. *Structural Optimization*, 1:193–202, 01 1989.

M. Bonnet, R. Cornaggia, and B. B. Guzina. Microstructural topological sensitivities of the second-order macroscopic model for waves in periodic media. *SIAM J. Appl. Math.*, 78(4): 2057–2082, 2018.

M. Briane and M. Camar-Eddine. An optimal condition of compactness for elasticity problems involving one directional reinforcement. *J. Elasticity*, 107(1):11–38, 2012.

V. Calisti. *Synthèse de microstructures par optimisation topologique, et optimisation de forme d'un problème d'interaction fluide-structure.* PhD thesis, 2021. Thèse de doctorat dirigée par Scheid, Jean-François et Ganghoffer, Jean-François Mathématiques Université de Lorraine 2021.

V. Calisti, A. Lebée, A. A. Novotny, and J. Sokołowski. Sensitivity of the second order homogenized elasticity tensor to topological microstructural changes. *J. Elasticity*, 144(2):141–167, 2021.

M. Camar-Eddine and P. Seppecher. Determination of the closure of the set of elasticity functionals. *Arch. Ration. Mech. Anal.*, 170(3):211–245, 2003.

R. Cornaggia and C. Bellis. Tuning effective dynamical properties of periodic media by fft-accelerated topological optimization. *International Journal for Numerical Methods in Engineering*, 121(14):3178–3205, 2020.

B. Durand, A. Lebée, P. Seppecher, and K. Sab. Predictive strain-gradient homogenization of a pantographic material with compliant junctions. *Journal of the Mechanics and Physics of Solids*, page 104773, 2022.

H. Eschenauer, V. Kobelev, and A. Schumacher. Bubble method for topology and shape optimization of structures. *Structural Optimization*, 8:42–51, 08 1994.

S. Forest. *Milieux continus généralisés et matériaux hétérogènes.* Presses des MINES, 2006.

S. Garreau, P. Guillaume, and M. Masmoudi. The topological asymptotic for PDE systems: the elasticity case. *SIAM Journal on Control and Optimization*, 39(6):1756–1778, 2001.

S. Giusti, P. Blanco, E. de Souza Neto, and R. Feijóo. An assessment of the gurson yield criterion by a computational multi-scale approach. *Engineering Computations*, 26:281–301, 04 2009a.

S. M. Giusti, A. A. Novotny, E. A. de Souza Neto, and R. A. Feijóo. Sensitivity of the macroscopic elasticity tensor to topological microstructural changes. *Journal of the Mechanics and Physics of Solids*, 57(3):555–570, 2009b.

L. Jakabčin and P. Seppecher. On periodic homogenization of highly contrasted elastic structures. *J. Mech. Phys. Solids*, 144:104104, 18, 2020.

C. McMahan, A. Akerson, P. Celli, B. Audoly, and C. Daraio. Effective continuum models for the buckling of non-periodic architected sheets that display quasi-mechanism behaviors. *Journal of the mechanics and physics of solids*, 166:104934–, 2022.

G. W. Milton. Complete characterization of the macroscopic deformations of periodic unimode metamaterials of rigid bars and pivots. *Journal of the Mechanics and Physics of Solids*, 61 (7):1543–1560, 2013.

A. A. Novotny and J. Sokołowski. *Topological derivatives in shape optimization*. Interaction of Mechanics and Mathematics. Springer, Heidelberg, 2013.

A. A. Novotny and J. Sokołowski. *An introduction to the topological derivative method*. Springer Briefs in Mathematics. Springer Nature Switzerland, 2020.

A. A. Novotny, J. Sokołowski, and A. Żochowski. *Applications of the topological derivative method*, volume 188 of *Studies in Systems, Decision and Control*. Springer, Cham, 2019. With a foreword by Michel Delfour.

A. A. Novotny, S. M. Giusti, and S. Amstutz. Guest Editorial: On the topological derivative method and its applications in computational engineering. *Engineering Computations*, 39(1): 1–2, 2022.

S. Osher and J. A. Sethian. Fronts propagating with curvature-dependent speed: algorithms based on Hamilton-Jacobi formulations. *J. Comput. Phys.*, 79(1):12–49, 1988.

G. Rosi and N. Auffray. Anisotropic and dispersive wave propagation within strain-gradient framework. *Wave Motion*, 63:120–134, 2016.

G. I. N. Rozvany. A critical review of established methods of structural topology optimization. *Struct. Multidiscip. Optim.*, 37(3):217–237, 2009.

A. Schumacher. *Topologieoptimierung von Bauteilstrukturen unter Verwendung von Lochpositionierungskriterien*. PhD thesis, Inst. für Mechanik und Regelungstechnik, 1996.

P. Seppecher, J.-J. Alibert, and F. D. Isola. Linear elastic trusses leading to continua with exotic mechanical interactions. In *Journal of Physics: Conference Series*, volume 319, page 012018. IOP Publishing, 2011.

O. Sigmund and K. Maute. Topology optimization approaches. *Struct. Multidiscip. Optim.*, 48 (6):1031–1055, 2013.

V. P. Smyshlyaev and K. D. Cherednichenko. On rigorous derivation of strain gradient effects in the overall behaviour of periodic heterogeneous media. *J. Mech. Phys. Solids*, 48:1325–1357, 2000. The J. R. Willis 60th anniversary volume.

J. Sokołowski and A. Żochowski. On the topological derivative in shape optimization. *SIAM Journal on Control and Optimization*, 37(4):1251–1272, 1999.

N. P. van Dijk, K. Maute, M. Langelaar, and F. van Keulen. Level-set methods for structural topology optimization: a review. *Struct. Multidiscip. Optim.*, 48(3):437–472, 2013.

M. Wallin, M. Ristinmaa, and H. Askfelt. Optimal topologies derived from a phase-field method. *Struct. Multidiscip. Optim.*, 45(2):171–183, 2012.

F. Wang, O. Sigmund, and J. S. Jensen. Design of materials with prescribed nonlinear properties. *J. Mech. Phys. Solids*, 69:156–174, 2014.

M. Zhou and G. Rozvany. The coc algorithm, part ii: Topological, geometrical and generalized shape optimization. *Computer Methods in Applied Mechanics and Engineering*, 89(1):309–336, 1991. Second World Congress on Computational Mechanics.

(V. Calisti) Institute of Mathematics of the Czech Academy of Sciences, Žitná 25, 115 67 Praha 1, Czech Republic, and, Institut Élie Cartan de Lorraine, UMR 7502, Université de Lorraine, B.P. 70239, 54506 Vandoeuvre-lès-Nancy Cedex, France.
Email address: calisti@math.cas.cz

(A. Lebée) Laboratoire Navier, UMR 8205, École des Ponts ParisTech, Université Gustave Eiffel, CNRS, Champs-sur-Marne, France
Email address: arthur.lebee@enpc.fr

(A.A. Novotny) Laboratório Nacional de Computação Científica LNCC/MCT, Coordenação de Métodos Matemáticos e Computacionais, Av. Getúlio Vargas 333, 25651-075 Petrópolis - RJ, Brasil
Email address: novotny@lncc.br

(J. Sokolowski) Systems Research Institute of the Polish Academy of Sciences, ul. Newelska 6, 01-447 Warszawa, Poland and, Department of Scientific Computing, Informatics Center, Federal University of Paraiba, Brazil, and, Institut Élie Cartan de Lorraine, UMR 7502, Université de Lorraine, B.P. 70239, 54506 Vandoeuvre-lès-Nancy Cedex, France
Email address: jan.sokolowski@univ-lorraine.fr